A metabolic model based on a pangenome core unveils new biochemical features of the phytopathogen *Xylella fastidiosa*

Corbín-Agustí, Paola[1*]; Álvarez-Herrera, Miguel[1]; Román-Écija, Miguel[2]; Álvarez, Patricia[1] ; Tortajada, Marta[3]; Landa, Blanca B.[2*]; Peretó, Juli[1,4]

[1]Institute for Integrative Systems Biology, I2SysBio (CSIC-Universitat de València), Paterna, Spain.

[2]Institute for Sustainable Agriculture (IAS), Spanish National Research Council (CSIC), Córdoba, Spain.

[3]Department of Biomedical Sciences, Faculty of Health Sciences, Universidad Cardenal Herrera, Centro de Estudios Universitarios, UCH-CEU, Alfara del Patriarca, Spain.

[4]Department of Biochemistry and Molecular Biology, University of Valencia, Burjassot, Spain.

*Corresponding authors: Blanca B. Landa blanca.landa@ias.csic.es, Paola Corbín Agustí paola.corbin@uv.es

Abstract

Xylella fastidiosa is a xylem-limited phytopathogen bacterium responsible for severe diseases in numerous plant species of major agricultural importance. Despite its economic impact, its metabolism remains poorly characterized due to the bacterium's fastidious growth and the limited availability of defined culture media. In this work, we reconstructed the first pangenome-based genome-scale metabolic model for *X. fastidiosa*, integrating the conserved metabolic capabilities of 18 strains representing five described subspecies. The resulting core metabolic model, Xfcore, was manually curated and used to investigate the metabolic potential of the species. Model simulations predict minimal nutritional requirements that guide the formulation of defined media capable of supporting biofilm formation in vitro. Analysis of the metabolic network also suggests an undescribed metabolic pathway that enables growth on acetate as a sole carbon source. Furthermore, the model predicts that *X. fastidiosa* could overproduce polyamines, compounds previously associated with virulence in other phytopathogens. Experimental analyses confirm the production and secretion of polyamines in several *X. fastidiosa* strains, providing the first in vitro evidence of polyamine production in this pathogen. These findings suggest that polyamine biosynthesis may represent an uncharacterized virulence factor in *X. fastidiosa*, potentially contributing to bacterial protection against host-induced oxidative stress. Overall, the Xfcore model provides a systems-level framework to explore the metabolism of *X. fastidiosa*, generate testable hypotheses about its physiology and virulence, and establish a basis for future strain-specific reconstructions and host-pathogen metabolic interaction studies.

Keywords: *Xylella fastidiosa* pangenome, metabolic model, polyamines, acetate metabolism, defined medium

Introduction

Xylella fastidiosa is a fastidious, Gram-negative, xylem-limited phytopathogenic bacterium that infects more than 700 plant species worldwide (EFSA et al., 2026), including several crops of major agro-economic relevance. In some of these hosts, the bacterium causes devastating diseases such as Pierce's disease (PD) in grapevine, citrus variegated chlorosis (CVC), almond leaf scorch (ALS), and olive quick decline syndrome (OQDS). The bacterium colonizes the xylem vessels of its plant hosts, and symptoms development depends on several bacterial virulence factors, particularly the formation of biofilm and host defense responses (Landa et al., 2022; De La Fuente et al., 2024). Biofilms also develop in the anterior foregut of sap-feeding insect vectors, which mediate bacterial transmission (Chatterjee et al., 2008).

Xylella fastidiosa is also characterized by substantial intraspecific diversity. Recent computational analyses based on k-mer signatures support a revised taxonomy that groups the species into three major clades: clade I (corresponding to subsp. *pauca*), clade II (subsp. *multiplex*) and clade III (including three subsp.: *fastidiosa*, *morus* and *sandyi*) (Denancé et al., 2019). In parallel, multilocus sequence typing (MLST) has been widely used for the epidemiological characterization of isolates (Scally et al., 2005) and 90 sequence types (STs) have been described to date (Jolley et al., 2018; EPPO 2023). Although STs do not provide genome-wide resolution and therefore cannot capture the full extent of gene-content variation, they remain useful for rapid strain typing, subspecies assignment, and initial epidemiological interpretation. However, the high recombination rates and the existence of some non-monophyletic STs raise concerns about the phylogenetic resolution and the robustness of current classification schemes based solely on MLST (Hanage et al., 2005; Vanhove et al., 2019; Landa et al., 2020). This genomic complexity suggests that marker-based classification alone is insufficient to infer functional traits, including metabolic capabilities that may influence host association, niche adaptation, and pathogenicity (Landa et al., 2022).

Despite decades of research, key aspects of *X. fastidiosa* physiology –particularly those linked to virulence, host adaptation, and nutritional requirements– remain poorly understood. This knowledge gap is especially relevant because the bacterium inhabits the xylem, a nutritionally restricted environment in which successful colonization, multiplication, and biofilm formation are expected to depend strongly on metabolic adaptation. Its inability to grow efficiently on standard bacteriological media, reflected in the species epithet "*fastidiosa*", continues to be a defining feature of the species (Davis et al., 1981; Wells et al., 1987; Chatterjee et al., 2008). Empirical efforts have produced improved culture media that support faster growth (Davis et al., 1980; Wells et al., 1981; Davis et al., 1981), but none fully overcome its fastidiousness

(Campanharo et al., 2003). Moreover, growth in currently available defined media remains slow and biomass production is limited. As a result, the metabolic basis of nutrient use, physiological specialization, and virulence-associated traits in *X. fastidiosa* is still only partially resolved (De La Fuente et al., 2024).

Genome-scale metabolic models (GEMs) are structured knowledge bases that integrate biochemical, genetic and genomic data into a system-level representation of the metabolic capabilities of an organism (O'Brien et al., 2015). Over the past two decades, GEMs have been applied in systems biology, enabling in silico prediction of genotype-phenotype relationships, reverse ecology paradigm to infer ecological features from genomic data, such as nutrient requirements prediction and growth medium design, and the discovery of metabolic network properties or pan-reactome comparisons (Yus et al., 2009; Monk et al., 2014; Gu et al., 2019; Ye et al., 2022; Qian & Ye, 2024). Constraint-based reconstruction and analysis (COBRA) is one of the foundational and most widely used approaches for working with GEMs. It achieves high predictive power by imposing physicochemical and environmental constraints (such as stoichiometry, thermodynamics and nutrient availability) that define a solution space encompassing all feasible metabolic states of the cell under different conditions (Ibarra et al., 2002; Palsson, 2015).

Here, we present an in silico approach to investigate key aspects of *X. fastidiosa* physiology through the reconstruction of a GEM. Although two metabolic models have previously been reconstructed for this phytopathogen, both are strain-specific (Gerlin et al., 2020; Oliveira et al., 2023). In this study, to account for the genetic diversity within the species while focusing on its conserved metabolic functions, a pangenome was assembled and used it as the template for a core metabolic reconstruction. The resulting model represents a species-level GEM that reflects metabolic functions conserved across *X. fastidiosa,* rather than traits restricted to particular subspecies or strains. Then, the resulting reconstruction was experimentally validated by growth-phenotype profiling of a selection of *X. fastidiosa* strains via Biolog Phenotyping assays. We also used the model to design a defined minimal growth medium based on predicted nutritional requirements –an aspect that has received limited attention despite *X. fastidiosa* being the first phytopathogenic bacterium with a fully sequenced genome (de Macedo Lemos et al., 2003). Beyond this, exploration of the metabolic network highlighted two notable features of the bacterial physiology. First, given the absence in *X. fastidiosa* of previously described acetate assimilation pathways, we sought a metabolic solution that would explain growth on acetate as the sole carbon source. The resulting pathway emerges from the combination of submodules from other metabolic routes, providing genomic support for acetate utilization suggested by model-based analyses. Second, the

model predicts a remarkable capacity for polyamine biosynthesis. Polyamines are metabolites that are not only produced by plants as part of their oxidative stress and defense responses, but have also been previously linked to virulence in other phytopathogens such as *Ralstonia solanacearum* (Lowe-Power et al., 2018) and *Pseudomonas syringae* (Solmi et al., 2025). We experimentally confirmed polyamine production in *X. fastidiosa*, suggesting a possible role in host-pathogen interactions. Together, this work delivers the first species-level GEM of *X. fastidiosa* and establishes a systems biology framework to investigate its physiology, nutritional requirements, and metabolic determinants of pathogenicity.

Results

Metabolic characteristics of the *Xylella fastidiosa* pangenome and the core metabolic model

A curated genome-scale metabolic reconstruction was generated based on the core genes of 18 *X. fastidiosa* strains representing the subspecies *fastidiosa*, *pauca*, *multiplex*, *morus* and *sandyi* (Table 1), and including the strains previously used for metabolic modelling (Gerlin et al., 2020; Oliveira et al., 2023). These strains were isolated from a diverse set of host plants, including grapevine, almond, sweet orange, olive, coffee and several wild species. This host diversity reflects the broad ecological range of the species and provides a representative basis for assessing its pangenomic and metabolic variability. Moreover, this pangenome also incorporates recently emerged European strains, with six isolates from Spain, Italy and France, in order to account for the lineages involved in the outbreaks starting to be detected in 2013, which have resulted in substantial agricultural and economic losses in Europe (Sanchez et al., 2019; De la Fuente, 2024).

Pangenome analysis revealed a total of 2660 ortholog groups (OGs), comprising 40828 genes, of which 1372 OGs included genes found in the 18 strains (Fig. 1A). The core genome consists of 26831 genes, constituting 65.72% of the genes analyzed. The accessory genome includes 13421 genes, corresponding to 32.87% of the total pangenome. Among the analyzed strains, XYL468 exhibited the highest number of accessory genes (890), whereas Salento-1 displayed the lowest (595). A total of 576 genes were classified as unique, accounting for 1.41% of all genes. The strain with the largest number of unique genes was XYL1961/18, with 141 unique genes, while U24D contained only 2 unique genes. Only a limited number of OGs showed strict subspecies-specific distribution.

140 Functional annotation of the pangenome revealed clear differences between the core,
141 accessory, and unique gene sets (Fig. S1). Core ortholog groups were predominantly enriched
142 in metabolic functions, particularly carbohydrate, amino acid, nucleotide, energy and glycan
143 metabolism, as well as metabolism of cofactors and vitamins. These were followed in
144 prevalence by genes associated with genetic information processing and with signalling and
145 cellular processes. In contrast, accessory genes showed a stronger representation of the latter
146 two categories, including a higher proportion of functions associated with prokaryotic defense
147 systems, secretion and transport systems, and quorum-sensing pathways, alongside a
148 substantial fraction of genes with unknown function. Metabolic genes were also present within
149 the accessory set, although to a lesser extent. For the unique gene set, only 6.2% (36 out of
150 576) of the genes could be functionally annotated, and none were linked to core metabolic
151 pathways. Instead, the annotated genes mapped to categories such as prokaryotic defense
152 systems, quorum sensing, or DNA replication and repair.

153 The core ortholog set identified in the pangenome analysis was used to generate a draft
154 genome-scale metabolic reconstruction using the automated reconstruction software
155 ModelSEED (Henry et al., 2010). Curation was performed iteratively. Initial efforts focused on
156 central metabolism and biomass production. Subsequently, complete biosynthetic routes for
157 amino acids, lipids, nucleotides, energy metabolism, and selected transport systems were
158 manually reviewed. Pathways associated with redox balance, cofactor biosynthesis, and host-
159 associated growth were carefully curated, including quinone and shikimate biosynthesis,
160 polyamine metabolism, the S-adenosylmethionine (SAM) cycle, sulfur and nitrogen
161 metabolism, and the methionine salvage pathway. Vitamin and cofactor biosynthetic pathways
162 were curated in detail, encompassing pantothenate, folate, riboflavin, thiamine, and porphyrin
163 metabolism. Finally, pathways associated with cell envelope biogenesis and host interaction
164 were refined, including exopolysaccharide (EPS) and lipopolysaccharide (LPS) biosynthesis,
165 as well as fatty acid metabolism, and the biosynthesis and export of the LesA protein, following
166 previous strain-specific metabolic reconstructions (Gerlin et al., 2020; Oliveira et al., 2023).

167 During this iterative process, a set of accessory genes were identified as present in the
168 majority of the strains, and considered relevant for modelling the general metabolic behavior
169 of *X. fastidiosa* (Table S1). These genes were not included into the core set of sequences due
170 to pseudogenization events in specific strains. In several cases, this was the result from
171 frameshift mutations caused by single-nucleotide insertions or deletions within repetitive
172 nucleotide regions, which may allow some enzymatic activity or reflect sequencing artefacts
173 (Cooley & Wright, 2024). For instance, the accessory gene XF_RS10205, encoding 5'-
174 methylthioadenosine phosphorylase, is annotated as a pseudogene in strain 9a5c despite

175 being reviewed in UniProt (Q9PAZ2) as a functional enzyme. In total, 43 accessory genes
176 were incorporated into the metabolic reconstruction.

177 The final genome-scale metabolic reconstruction (Xfcore; Supplementary Material S1)
178 included 1034 reactions, 1075 metabolites (corresponding to 1013 unique metabolites), 451
179 genes, and two cellular compartments: cytoplasm and extracellular space (Fig. 1B). Of the
180 metabolites, there were 63 extracellular and 1012 cytosolic. The model includes 69 boundary
181 reactions (exchange, sink, and demand reactions), and 76 transport reactions enabling
182 metabolite exchange between compartments. Among the 451 genes, 407 belong to the core
183 pangenome, while 43 are accessory genes (Table S1). Additionally, there is a gene called
184 "Unknown", indicating a functional requirement in the network despite the absence of genetic
185 evidence. A total of 83% of reactions (859 out of 1034) are associated with gene-protein-
186 reaction (GPR) rules. Of the 175 reactions lacking GPR associations, 99 correspond to
187 boundary or transport reactions, the majority of which do not require gene assignment. Model
188 quality and consistency evaluated using the Memote testing suite (Lieven et al., 2020), yielded
189 a total score of 85% and a consistency score of 97% (Supplementary Material S2). Annotation
190 completeness scores were 66% for metabolites, 73% for reactions, and 53% for genes. The
191 coverage of SBO terms reached 83%, indicating strong semantic and structural annotation.

192 The core gene set of *X. fastidiosa* encoded nearly all central metabolic functions, although
193 several specific gaps and distinctive features were identified. The Embden-Meyerhof-Parnas
194 (EMP) and the Entner-Doudoroff (ED) glycolytic pathways were fully represented in the model.
195 However, one enzyme from the gluconeogenic pathway –namely, fructose-1,6-
196 bisphosphatase (FBPase)– was not identified in any gene set of the pangenome. This
197 absence would suggest limitations in the performance of gluconeogenesis. Nevertheless,
198 extensive experimental evidence indicates that *X. fastidiosa* is capable of converting pyruvate
199 into sugars (Davis et al., 1980, 1981; Almeida et al., 2004; Gerlin et al., 2020). As previously
200 proposed by Oliveira et al. (2023), FBPase activity (EC 3.1.3.11) can be functionally replaced
201 by a reversible pyrophosphate-dependent phosphofructokinase (PPi-PFK; EC 2.7.1.90),
202 encoded by gene XF_RS01160. This enzyme, homologous to the PPi-PFK described in
203 *Xanthomonas campestris* (UniProt: B0RP51), is reversible and can therefore catalyze both
204 the forward glycolytic reaction and the reverse gluconeogenic conversion. Accordingly, this
205 reaction was implemented in the model to account for both activities.

206 The oxidative and non-oxidative branches of the pentose phosphate pathway (PPP) were
207 evaluated in the core gene set. Glucose-6-phosphate dehydrogenase (EC 1.1.1.49) –an
208 enzyme shared with the ED pathway– was present in all strains except Pr8x, where it appears

209 as a pseudogene; nevertheless, this activity was retained in the model to reflect its functional
210 relevance. Two additional activities were absent from the core pangenome: 6-
211 phosphogluconate dehydrogenase (PPP oxidative phase) and transaldolase (TALA, PPP non-
212 oxidative phase). Although the absence of the oxidative branch of the pentose phosphate
213 pathway prevents NADPH generation through this route, reducing power may be supplied by
214 the ED pathway and additional reactions such as the malic enzyme. No transhydrogenase
215 activity was identified in the model. Flux redistribution through the reversible reactions of the
216 PPP non-oxidative branch allows synthesis of essential precursors such as phosphoribosyl
217 pyrophosphate (PRPP). In contrast, the absence of TALA is expected to impair growth on
218 pentoses as sole carbon sources, as it disrupts sedoheptulose-7-phosphate (S7P)
219 metabolism. In previously published models (Oliveira et al., 2023), growth on ribose was
220 enabled by incorporating a sedoheptulose-1,7-bisphosphate (SBP) bypass reaction that
221 converts S7P into SBP using PPi instead of ATP, and subsequently cleaved into
222 dihydroxyacetone phosphate (DHAP) and erythrose-4-phosphate (E4P). Experimental and
223 computational studies have shown that bacteria lacking TALA can metabolize S7P through an
224 SBP aldolase pathway (Nakahigashi et al., 2009; Koendjbiharie et al., 2020; Garschagen et
225 al., 2021). For the phosphorylation step, we assigned this activity to the pyrophosphate-
226 dependent phosphofructokinase (PPi-PFK; XF_RS01160), which has been shown in other
227 bacteria to catalyze reversible PPi-dependent phosphoryl transfer reactions (Koendjbiharie et
228 al., 2020). For the aldolase reaction, which converts SBP to DHAP and E4P, we hypothesized
229 that the fructose-bisphosphate aldolase encoded by XF_RS03490 may exhibit substrate
230 promiscuity and catalyze both FBP and SBP cleavage. Such dual specificity has been
231 described in other bacteria, including *Synechocystis* sp. PCC 6803, where class I and II
232 aldolases can participate in SBP metabolism in MetaCyc.

233 Every enzymatic step of the tricarboxylic acid (TCA) cycle was represented within the core
234 pangenome. The oxoglutarate dehydrogenase complex (ODC) was supported by all its
235 subunits, although the E1 component (XF_RS06555) was absent in strain 3124. The E2
236 component (XF_RS06550) was conserved in the core genome. The pyruvate dehydrogenase
237 complex (PDC), which catalyzes an analogous reaction and shares a similar multienzyme
238 architecture with ODC, showed strain-specific variation in the E2 subunit. The gene encoding
239 the E2 component (XF_RS03665; dihydrolipoyllysine-residue acetyltransferase) was
240 annotated as a pseudogene in strains XYL468 and CFBP8418, however, inconsistencies
241 between genome assemblies in NCBI suggest potential sequencing or annotation artefacts.
242 So, this complex was conserved in the metabolic model. Two candidate genes encoding the
243 E3 subunit (dihydrolipoyl dehydrogenase) were identified in the pangenome (XF_RS06540

244 and XF_RS03660). Only XF_RS06540 was part of the core gene set and was therefore
245 assigned as the shared E3 component for both ODC and PDC in the model. Importantly, no
246 enzymes associated with the glyoxylate shunt were identified in any analyzed strain.

247 Remarkably, pyruvate carboxylase (EC 6.4.1.1), which catalyzes the ATP-dependent
248 conversion of pyruvate to oxaloacetate (OAA), was not identified in the *X. fastidiosa*
249 pangenome and was therefore not included in the model. No alternative reaction directly
250 linking pyruvate to oxaloacetate was detected. The absence of this anaplerotic step limits the
251 replenishment of tricarboxylic acid (TCA) cycle intermediates when sugars or organic acid
252 compounds are supplied as sole carbon sources. Under these conditions, growth requires
253 TCA intermediates to sustain biosynthetic demands. The reconstructed network lacks
254 sufficient anaplerotic reactions to compensate for carbon withdrawal from the cycle, resulting
255 in growth impairment in silico. To evaluate whether growth could be sustained using plant
256 metabolites, we considered incorporating TCA cycle intermediates or their precursors –e.g.,
257 glutamine or glutamate– which could be supplied by the host, to simulate bacterial growth.

258 As previously described, the core metabolic network of *X. fastidiosa* contained complete
259 biosynthetic pathways for all amino acids. Lipid biosynthesis pathways were also identified
260 and included in the reconstruction, whereas no evidence of lipid degradation pathways –e.g.,
261 fatty acids β-oxidation– was detected in the pangenome. Additionally, no auxotrophies were
262 identified for essential vitamins or cofactors.

263 As for quinone-dependent electron transport, only the ubiquinone biosynthetic pathway was
264 identified in the pangenome, although it appeared incomplete. No candidate gene was
265 detected for two intermediate reactions corresponding to the decarboxylation and
266 hydroxylation of 3-polyprenyl-4-hydroxybenzoate. Nevertheless, the upstream and
267 downstream steps of the pathway were conserved, and no alternative quinone biosynthetic
268 route was identified. Given the apparent continuity of the pathway and the absence of
269 pseudogenization in adjacent enzymatic steps, it is likely that these missing reactions are
270 catalyzed either by highly divergent enzymes not detected by sequence homology, by
271 promiscuous enzymatic activities, or through non-canonical mechanisms that remain to be
272 characterized.

273 Finally, the biomass reaction was formulated to include all known cellular components and
274 their respective contributions per gram of biomass. Following extensive curation, including
275 comparative evaluation against the biomass formulations of the *Escherichia coli* model
276 iJO1366 (Orth et al., 2011) and the *X. fastidiosa* model Xfm1158 (Gerlin et al., 2020), the
277 biomass equation included 78 metabolites.

278 Flux balance analysis (FBA) predicted a maximum specific growth rate of 0.413 h^{-1} when
279 glutamine, one of the major components of xylem sap, was supplied as the sole carbon source
280 at an uptake rate of 7.25 $mmol \cdot gDW^{-1} \cdot h^{-1}$ (Supplementary Material S3). The corresponding
281 optimal flux distribution is shown in Fig. 1C. Under these conditions, most of the imported
282 glutamine is first converted into glutamate and subsequently into α-ketoglutarate, which enters
283 the tricarboxylic acid (TCA) cycle. Carbon flux proceeds through the cycle to generate malate
284 and oxaloacetate. Malate is partially converted to pyruvate via the malic enzyme, generating
285 NADPH and contributing to cellular reducing power. Pyruvate is then redirected toward
286 gluconeogenesis to supply precursors required for lipid, cell wall, and other biomass
287 components. In parallel, a fraction of pyruvate is converted into acetyl-CoA, which supports
288 fatty acid biosynthesis and citrate formation, ultimately reconnecting with α-ketoglutarate
289 within the TCA cycle. The Xfcore model further predicted uptake of inorganic ions, phosphate,
290 and sulfate under these growth conditions, while CO_2 and NH_3 were secreted as metabolic
291 by-products. Oxygen was also required, as the model did not predict growth under anaerobic
292 conditions.

293

294 Experimental validation of the metabolic reconstruction

295 Phenotypic characterization of *Xylella fastidiosa* strains

296 The phenotypic characterization of strains ESVL, De Donno, IVIA5901, Temecula1 and
297 XYL1961/18 using the phenotype microarray system of Biolog (Supplementary Material S4,
298 Figs. S2 and S3) showed partially overlapping metabolic fingerprints. Among strains, De
299 Donno showed the highest proportion of assimilated carbon sources (31.6% and 38.9% for
300 PM1 and PM2, respectively), whereas Temecula1 showed the lowest (26.3% and 21.1%,
301 respectively) (Table S2). Overall, the five strains consistently metabolized 34 out of the 190
302 compounds tested (17.9%): 17 compounds in PM1 and 17 compounds in PM2 plates (Table
303 2; Fig. S4 and S5). Additionally, five compounds were classified as exhibiting “Undetermined”
304 growth across all strains, due to positive growth in only two of the four biological replicates. In
305 contrast, 50 compounds were not assimilated by any of the strains (Supplementary Material
306 S4; Figs. S4 and S5).

307 The main groups of compounds consistently utilized as carbon sources by all *X. fastidiosa*
308 strains in the PM1 and PM2 plates included i) carbohydrates and their derivatives, ii) organic
309 acids, iii) lipids and fatty acids, and iv) amino acids derivatives and amines. These in vitro

310 results were compared with in silico growth predictions for each compound, when possible
311 (Table 2, Supplementary Material S5).

312 In silico predictions were consistent with in vitro results for 7 out of the 34 metabolites that
313 supported growth in vitro (D-ribose, D-xylose, D-fructose-6-phosphate, D-glucosamine, α-
314 ketoglutaric acid, pyruvic acid, and acetic acid) (Table 2, Supplementary Material S5).
315 Nineteen out of the 34 metabolites could not be evaluated using the Xfcore model because
316 they were not included in the reconstructed metabolic network or their metabolism could not
317 be represented. These included all lipids and fatty acids, as well as amino acid derivatives and
318 amines. For the remaining eight metabolites, growth was observed in vitro but could not be
319 supported in silico (L-arabinose, L-lyxose, 2-deoxy-D-ribose, D-psicose, D-tagatose, α-
320 ketobutyric acid, acetoacetic acid, and dihydroxyacetone).

321 Additionally, several compounds that did not support growth for all strains in the PM plates
322 were evaluated in silico due to their reported abundance in the xylem sap of olive, almond,
323 and citrus trees (Table 2, Supplementary Material S5) (Youssefi et al., 2000; Purcino et al.,
324 2007; Anguita-Maeso et al., 2021; Fausto et al., 2021; Surano et al., 2024). D-glucose, one of
325 the major sugars detected in olive xylem sap, was predicted to sustain growth in silico,
326 consistent with previous strain-specific models (Gerlin et al., 2020; Oliveira et al., 2023).
327 However, this prediction was not supported experimentally, as only one strain showed
328 undetermined growth while the remaining four exhibited no growth in the PM assays (Fig. S4).
329 Citric acid, also reported as a common organic acid in xylem sap, was predicted to sustain
330 growth in silico. The corresponding transporter was present in the core pangenome, and
331 growth has been supported in other reconstructions. Experimentally, citrate supported growth
332 in one strain, showed indeterminate growth in one strain, and resulted in no growth in the
333 remaining three strains.

334 Regarding amino acids commonly reported in xylem sap (glutamine, glutamate, aspartate,
335 arginine, asparagine, alanine, serine, and proline), in silico simulations predicted growth on L-
336 glutamine, L-glutamate, L-aspartate, and L-alanine (Table 2, Supplementary Material S5).
337 However, experimental validation showed partial or limited agreement (Fig. S4 and S5). L-
338 aspartate supported growth in vitro in two strains, while one strain showed undetermined
339 growth and two showed no growth. In contrast, L-glutamate, L-glutamine, and L-alanine
340 predominantly resulted in undetermined or no-growth phenotypes across strains despite being
341 predicted to sustain growth in silico. L-arginine, L-asparagine, L-serine, and L-proline were not
342 predicted to support growth in silico. Consistently, these amino acids did not sustain robust
343 growth in vitro, with most strains showing either no growth or undetermined phenotypes.

344

345 **Growing *Xylella fastidiosa* in minimal media predicted by the model**

346 Empirical efforts have led to the development of several culture media for *X. fastidiosa*,
347 including PD2 (Davis et al., 1980), BCYE (Wells et al., 1981) and PW (Davis et al., 1981).
348 However, these formulations do not fully overcome the fastidious growth requirements of the
349 bacterium. In this work, a reverse ecology approach based on constraint-based metabolic
350 modeling was applied to predict a synthetic defined minimal medium capable of sustaining
351 biomass production in the Xfcore model. Under a fixed L-glutamine uptake constraint (7.25
352 $mmol \cdot gDW^{-1} \cdot h^{-1}$), the minimal medium prediction identified oxygen, phosphate, sulfate,
353 glutamine (as both carbon and nitrogen source), and inorganic ions as required components
354 (see Supplementary Material S6 for the complete list of metabolites and corresponding uptake
355 fluxes).

356 Based on these predicted requirements, six synthetic defined minimal media were formulated
357 (mXC1–mXC6; Table S3). Glutamine was used as the sole carbon and nitrogen source in
358 mXC1 and mXC2, given its abundance in xylem sap, despite not supporting growth in the
359 phenotypic characterization plates. Two different iron sources were tested in these media,
360 ferric pyrophosphate and hemin chloride, to assess iron bioavailability. Acetate was used as
361 the carbon source in mXC3 and mXC4, supplemented with ammonium sulfate as a nitrogen
362 source. To validate model predictions regarding biotin dependency under acetate growth
363 conditions (see below Acetate metabolism section), mXC4 was additionally supplemented
364 with biotin. Finally, ribose was tested as the sole carbon source in mXC5 and mXC6. In mXC6,
365 cysteine was evaluated as an alternative nitrogen source, as it showed strong utilization in
366 nitrogen assimilation assays (Biolog PM3 plate; data not shown).

367 All minimal media supported, to some extent, the growth and biofilm formation in all *X.*
368 *fastidiosa* strains studied (Fig. 2; Supplementary Material S6). Interestingly, all strains were
369 able to grow with glutamine media, despite glutamine not supporting growth in the previous
370 phenotypic characterization of Biolog PM plates. The reference medium PD3 significantly
371 supported higher sAUGPC values than all minimal media across strains (Fig. 2A), except for
372 XYL1961/18, which showed higher growth in the Glutamine+Fe formulation (mXC1) and no
373 significant differences were detected for the rest of the media. In strain XYL468, no significant
374 differences were observed between PD3 and Glutamine+Hemin or Ribose+Cysteine media.
375 sAUGPC values in PD3 ranged from 0.002±0.0011 to 0.072±0.1344, being between 3.3 to
376 58.4-fold higher than those obtained in the minimal media.

377 On the other hand, biofilm formation (Fig. 2B) showed comparable levels across most minimal
378 media relative to PD3. The exception was strain De Donno, which produced significantly
379 higher biofilm in the control medium (PD3). Strain IVA5901 exhibited enhanced biofilm
380 formation in Ribose+NH_4 compared to PD3. Overall, a general trend was observed in which
381 synthetic defined media containing ribose supported higher biofilm production across most
382 strains, followed by acetate-based media.

383 Pairwise comparisons between media formulations sharing the same carbon source revealed
384 no significant differences for growth or biofilm formation associated with iron source, biotin
385 supplementation in acetate media, or nitrogen source substitution in ribose-based
386 formulations (data not shown).

387

388 **Acetate metabolism in *Xylella fastidiosa***

389 Experimental evidence supports the ability of *X. fastidiosa* to grow on acetate as the sole
390 carbon source in several strains (Gerlin et al., 2020; this work). In this work, all previously
391 described metabolic solutions to produce biomass from acetate were evaluated (see Material
392 and Methods). These included: i) the glyoxylate cycle (Kornberg & Krebs, 1957); ii) a
393 ferredoxin-dependent pyruvate synthase (Segura et al., 2008), typically associated with
394 anaerobic metabolism; iii) the ethylmalonyl-CoA (EMC) pathway (Erb et al., 2007); iv) the
395 methylaspartate cycle (MaC) characteristic of haloarchaea (Khomyakova et al., 2011); and v)
396 part of the 3-hydroxypropionate (3HP) autotrophic bi-cycle (Herter et al., 2002). Across the
397 18 strains comprising the pangenome, none of these previously described pathways were fully
398 supported by genomic evidence, lacking all or some of the necessary enzymes for these
399 routes. Alternative glyoxylate and propionyl-CoA assimilation modules, including the
400 methylcitrate cycle (Brämer & Steinbüchel, 2001; Dolan et al., 2018), were also examined.

401 The Xfcore metabolic model predicted growth on acetate through an alternative, yet
402 undescribed metabolic solution (Fig. 3). This consisted of a modular pathway with 11 steps
403 (Table S4), connecting acetate to central carbon metabolism, generating pyruvate and
404 succinate and enabling net carbon assimilation into biomass. This pathway integrates two
405 enzymatic subsets present in previously described metabolic routes. The first one corresponds
406 to the initial half of the 3HP bi-cycle, linking acetyl CoA to the synthesis of propionyl-CoA (the
407 remaining reactions of the cycle are absent from the pangenome). The second subset
408 corresponds to the methylcitrate pathway, which enables the assimilation of propionyl-CoA
409 into pyruvate and succinate. During the reconstruction process, minor gaps were identified in

410 the draft network. These gaps were resolved through manual genome evaluation and literature
411 reviewing. All reactions included in the final pathway are supported by genes present in the
412 pangenome. Below we describe the route in more detail, indicating the specific steps shown
413 in Fig. 3.

414 First, acetate enters the cell through a sodium-dependent acetate symporter (XF_RS09795),
415 which is present in all strains analyzed. Subsequently, acetate is converted into acetyl-CoA
416 by acetate-CoA ligase (step 1; XF_RS09805). This gene is absent in the J1A12 strain due to
417 a single nucleotide deletion (loss of an adenine at position 1120) within a repetitive region of
418 adenine. Apart from this frameshift mutation, the sequence is identical to that found in the
419 remaining strains. In step 2, acetyl-CoA carboxylase catalyzes the ATP-dependent
420 carboxylation of acetyl-CoA to produce malonyl-CoA. This enzyme requires biotin as a
421 cofactor for its catalytic activity. Malonyl-CoA is then reduced to malonate semialdehyde (3-
422 oxopropanoate; step 3) by a NADP-dependent malonyl-CoA reductase. Although the
423 associated gene (XF_RS05765) is annotated as aspartate semialdehyde dehydrogenase,
424 BLAST analysis and Pfam domain architecture match the reviewed UniProt entry A4YEN2
425 from *Metallosphaera sedula*, which performs this specific reaction. Step 4 involves the
426 conversion of malonate semialdehyde to 3-hydroxypropionate, catalyzed by 3-
427 hydroxypropionate dehydrogenase. This reaction was incorporated into the model and
428 assigned to gene XF_RS00605, annotated as NADP-dependent 3-hydroxy acid
429 dehydrogenase. In step 5, 3-hydroxypropionate is converted into its corresponding CoA-
430 activated form by an acyl-CoA synthetase, again encoded by XF_RS09805. In this case,
431 BLAST analysis and Pfam domain architecture matched the reviewed UniProt entry A4YGR1
432 from *M. sedula*, which catalyzes this specific reaction. This enzyme, annotated as “acs” in
433 several strains, would exhibit substrate flexibility, being also responsible for acetate activation.
434 Step 6 involves the dehydration of 3-hydroxypropionyl-CoA to acryloyl-CoA, catalyzed by an
435 enoyl-CoA hydratase, operating in the reverse direction. Although the candidate gene
436 XF_RS04720 identified did not yield a strong BLAST match to experimentally characterized
437 acryloyl-CoA hydratases, it is annotated as an enoyl-CoA hydratase, consistent with the
438 proposed reaction. Furthermore, Pfam domain analysis revealed the presence of the
439 conserved ECH_1 domain, which is characteristic of enoyl-CoA hydratase family enzymes
440 and is found in all reference proteins associated with this activity. Step 7 corresponds to the
441 final reaction of the 3HP bi-cycle module, involving the conversion of acryloyl-CoA into
442 propionyl-CoA. This reaction is catalyzed by an NADPH-dependent acryloyl-CoA reductase.
443 Two candidate genes belonging to the same orthologous group were identified as potentially
444 responsible for this activity (XF_RS07485 and XF_RS10335), both annotated as NAD(P)-

445 dependent alcohol dehydrogenases. BLAST analysis showed that XF_RS07485 matched the
446 reviewed UniProt entry A4YGN2 from *M. sedula*.

447 Propionyl-CoA is the metabolic junction between the module of part of 3HP bi-cycle and the
448 putative second module of the acetate assimilation, namely, the methylcitrate cycle. Step 8
449 corresponds to the condensation of propionyl-CoA with oxaloacetate to form 2-methylcitrate.
450 This reaction is classically catalyzed by methylcitrate synthase (PrpC). No canonical *prpC*
451 gene was identified in the core genome. However, the gene XF_RS06495, which is conserved
452 across all strains, annotated as citrate synthase (GltA), was identified as a potential candidate
453 for this step. Given this structural homology and the absence of a dedicated *prpC* gene, GltA
454 was considered the most parsimonious candidate to catalyze the condensation of propionyl-
455 CoA with oxaloacetate in the reconstructed pathway. Such substrate flexibility has been
456 reported for related enzymes within this family (for instance, *Bacillus subtilis*, UniProt entry
457 P45858, as reported in BRENDA database). Step 9 corresponds to the conversion of 2-
458 methylcitrate into 2-methylaconitate, which proceeds through two consecutive activities: 2-
459 methylcitrate dehydratase (EC 4.2.1.117; AcnD) followed by 2-methylaconitate *cis-trans*
460 isomerase (EC 5.3.3.7; PrpF). These transformations were included in the model as a
461 combined step. The *acnD* locus (XF_RS05260) was annotated as a pseudogene in a subset
462 of genomes (Temecula1, M23, 9a5c, U24D and Ann1). Among the strains used
463 experimentally, only Temecula1 carried this pseudogene annotation, whereas the remaining
464 experimental strains did not show this disruption. How this strain solves the absence of a
465 functional AcnD remains unsolved, and it would be worth studying the substrate promiscuity
466 of other aconitases. The gene *prpF* was identified in the core gene set of the pangenome
467 (XF_RS05265). Step 10 corresponds to aconitase AcnB, present in all strains and encoded
468 by XF_RS01240, and annotated as an aconitate hydratase 2 / 2-methylisocitrate dehydratase.
469 Finally, step 11 corresponds to methylisocitrate lyase (PrpB), which belongs to the core gene
470 set and is encoded by XF_RS05225, which produces pyruvate and succinate.

471 Compared with the flux distribution obtained when glutamine was used as the sole carbon
472 source (Fig. 1C), in the flux distribution corresponding to acetate assimilation (Fig. 3;
473 Supplementary Material S7) pyruvate is no longer converted into acetyl-CoA, as this
474 metabolite is directly generated from acetate (Fig. 3, step 1). The pyruvate generated in the
475 proposed pathway is redirected toward gluconeogenesis, similar to the glutamine-based
476 simulation. Under acetate conditions, the malic enzyme also contributes to NADPH
477 generation, although at 42% of the flux of the one observed with glutamine. This reduction
478 may seem a paradox since the acetate assimilation pathway proposed here shows an
479 increased demand of reducing power. A higher proportion of flux is directed through

480 oxaloacetate (95% vs 27.5% with glutamine). This increased TCA cycle flux implies a higher
481 flux through isocitrate dehydrogenase (IDH). The Xfcore model contains both the NAD- and
482 NADP-dependent IDH isozymes, and when the model was evaluated with pFBA under the
483 same conditions, with acetate 76% of the flux through IDH was generating NADPH, whereas
484 with glutamine as the only C source, all the flux went through the NAD-dependent IDH
485 isoenzyme.

486

487 **Polyamines production by *Xylella fastidiosa* strains**

488 As previously described for other phytopathogens, such as *R. solanacearum* and *P. syringae*
489 polyamine production could represent a potential virulence factor (Lowe-Power et al., 2018;
490 Solmi et al., 2025) that has not yet been characterized in *X. fastidiosa*. In the Xfcore metabolic
491 model, the biosynthesis pathways for the polyamines for putrescine, spermidine and spermine
492 were well represented, including the S-adenosylmethionine (SAM) regeneration cycle required
493 for the formation of spermidine and spermine biosynthesis (Fig. S6).

494 To evaluate the potential for polyamine overproduction, the presence of polyamine export
495 systems in *X. fastidiosa* was evaluated. Polyamines are positively charged at physiological pH
496 and therefore require active transport mechanisms to cross biological membranes. In *R.*
497 *solanacearum*, putrescine secretion has been experimentally reported (Lowe-Power et al.,
498 2018). However, no homologs of known polyamine exporters have been identified in its
499 genome (Igarashi & Kashiwagi, 2010; Sugiyama et al., 2017), suggesting the existence of a
500 yet uncharacterized transport system. In *X. fastidiosa*, no clear genomic evidence supporting
501 a dedicated polyamine export system was identified. Therefore, instead of assuming
502 extracellular exchange reactions, cytosolic demand reactions were introduced in the Xfcore
503 model to simulate polyamine overproduction.

504 When polyamine demand reactions were enforced or used as the objective function (see
505 Material and Methods), the model predicted feasible production of putrescine, spermidine, and
506 spermine, beyond biomass requirements (Fig. 4A). However, increasing polyamine production
507 resulted in a progressive reduction in biomass flux, revealing a trade-off between growth and
508 polyamine production. The extent of this trade-off varied among the three polyamines, with
509 differences in maximum achievable fluxes at minimum biomass levels. Under these
510 conditions, the model predicted maximum fluxes of 7.09 $mmol \cdot gDW^{-1} \cdot h^{-1}$ for putrescine, 1.57
511 $mmol \cdot gDW^{-1} \cdot h^{-1}$ for spermidine, and 0.87 $mmol \cdot gDW^{-1} \cdot h^{-1}$ for spermine, by individually
512 maximizing each polyamine demand reaction.

513 When putrescine overproduction was constrained to zero, spermidine and spermine exhibited
514 a linear inverse relationship, with limited flexibility concerning the production of biomass and
515 combined polyamine (Fig. 4A). In contrast, when putrescine overproduction was allowed
516 together with either spermidine or spermine, a broader feasible solution for similar biomass
517 levels space was observed. In these cases, similar biomass levels could be obtained with
518 different combinations of polyamine production, as reflected by the expansion of the biomass
519 contour levels.

520 The experimental results on polyamine production by *X. fastidiosa* strains corroborated the
521 findings of the Xfcore metabolic model (Fig 4B and Fig. S7; Supplementary Material S8). In a
522 first experiment (Fig. S7) six *X. fastidiosa* strains (De Donno, ESVL, IVIA5770, Temecula1,
523 XYL1961/18 and XYL468) produced and secreted polyamines in vitro. Putrescine, spermidine
524 and spermine were detected in cell pellets from both biofilm and planktonic growth (CP), as
525 well as in the culture supernatant (SP). Spermidine was produced at higher concentrations
526 than putrescine and spermine.

527 In a second experiment (Fig. 4B), polyamine levels were analyzed in three distinct sample
528 types: planktonic cell pellets (CP-P), biofilm-forming cell pellets (CP-B), and the culture
529 supernatant (SP). Again, spermidine was the most abundant polyamine produced. Mean
530 spermidine production across strains and time points ranged from 7.85±8.74 to 38.00±40.81
531 $ng \cdot mL^{-1}$ in CP-P and from 3.43±2.51 to 442.67±162.38 $ng \cdot mL^{-1}$ in CP-B. In SP, spermidine
532 levels ranged from 0 to 180.32±57.91 $ng \cdot mL^{-1}$. In contrast, mean putrescine values ranged
533 from 1.95±0.32 to 2.85±1.60 ng/ml in CP-P and from 1.67±0.31 to 5.18±1.01 $ng \cdot mL^{-1}$ in CP-
534 B, while SP values ranged from 0.24±0.27 to 5.65±3.40 $ng \cdot mL^{-1}$. Spermine production ranged
535 from 2.04±1.45 to 11.15±14.39 $ng \cdot mL^{-1}$ in CP-P, from 2.7±0.86 to 7.14±2.83 $ng \cdot mL^{-1}$ in CP-B,
536 and from 4.75±0.91 to 22.41±12.46 $ng \cdot mL^{-1}$ in SP.

537 There were no significant differences observed between time points within each sample type,
538 except for the four comparisons marked with an asterisk in Fig. 4B. Nevertheless, CP-B
539 samples showed an overall tendency for putrescine and spermidine to decrease between 5
540 and 12 days, a trend that was weaker and less consistent in CP-P. In the supernatant (SP),
541 spermidine showed the clearest evidence of extracellular accumulation, whereas putrescine
542 and spermine were also detected extracellularly but at lower levels. In some strains,
543 supernatant polyamine levels showed a tendency to increase at 12 days compared to 5 days.
544 Overall, these results indicate that spermidine is the most prevalent polyamine produced by
545 *X. fastidiosa* strains, suggesting that putrescine is converted into spermidine, which is then
546 further converted into spermine, but at a lower rate.

547

548 **Trade-off between virulence factors and biomass**

549 Previous reconstructions of *X. fastidiosa* metabolism (Gerlin et al., 2020; Oliveira et al., 2023)
550 have considered the secretion of two known virulence factors: the LesA protein (Nascimento
551 et al., 2016) and exopolysaccharides (EPS) (da Silva et al., 2001). The metabolic model of the
552 phytopathogen *R. solanacearum* (Peyraud et al., 2016), also incorporated polyamine
553 secretion due to its experimental confirmation.

554 To account for these virulence-associated processes, the Xfcore metabolic model
555 incorporated the reactions required for LesA biosynthesis. The gene responsible for LesA
556 production (XF_RS01515 or XF_RS01510) was present in the core gene set, and the ATP-
557 dependent transporter required for its export was also part of the core pangenome, with the
558 exception of one gene involved in the secretion cluster of strain J1A12 (XF_RS06440, *gspK*).
559 However, as described in other cases, the annotation of this gene as a pseudogene was due
560 to a deletion of a G at position 786 within a repetitive G-rich region.

561 For EPS biosynthesis, the *gum* operon responsible for EPS synthesis and export was found
562 in the core pangenome, with the exception of the *gumF* gene, which encodes an
563 acetyltransferase responsible for the final step of the biosynthetic pathway. This gene was
564 annotated as a pseudogene in strains U24D and Salento 2; however, since the rest of the
565 operon was present and the pseudogene annotation results from a single point mutation that
566 could represent a sequencing error, EPS production was incorporated into the Xfcore model.

567 In this work, several exploration scenarios were analyzed by simulating the combined
568 production of LesA protein, exopolysaccharides (EPS), and one of the polyamines: putrescine
569 (Fig. 5A), spermidine (Fig. 5B), or spermine (Fig. 5C). Under these conditions, the model
570 predicted maximum fluxes of 0.02 $mmol \cdot gDW^{-1} \cdot h^{-1}$ for LesA protein, 1.45 $mmol \cdot gDW^{-1} \cdot h^{-1}$ for
571 EPS, while the maximum achievable fluxes for putrescine, spermidine and spermine
572 correspond to those previously described.

573 In these simulations, a clear trade-off between virulence factor secretion and biomass
574 production was observed (Fig. 5). The combined production of LesA with EPS showed a linear
575 inverse relationship. For the production of putrescine together with the known virulence factors
576 (Fig. 5A), a nearly linear inverse relationship was observed between the combined production
577 of these compounds and biomass formation. Interestingly, in the case of spermidine (Fig. 5B)
578 and spermine (Fig. 5C), the feasible solution space showed greater compatibility between
579 LesA production and polyamine secretion. In these scenarios, different rates of LesA

580 production remain feasible even when spermidine or spermine are produced at high levels,
581 indicating greater metabolic flexibility for LesA secretion while maintaining the same biomass
582 flux. This behavior is reflected by the broader feasible region observed in the phase planes.
583 In particular, a change in slope appears when LesA production reaches approximately 0.02
584 $mmol \cdot gDW^{-1} \cdot h^{-1}$. A similar but less pronounced pattern is observed for EPS production.
585 Overall, EPS secretion appears to be more compatible with spermidine or spermine production
586 than with putrescine production, particularly near the upper limit of EPS flux (around 1.3
587 $mmol \cdot gDW^{-1} \cdot h^{-1}$).

588

589 # Discussion

590 In this work, we reconstructed the core metabolic model of *X. fastidiosa* based on the
591 pangenome of 18 strains, representing five described subspecies of the phytopathogen. This
592 approach accounts for the high genetic diversity within the species while allowing the
593 identification of conserved metabolic capabilities to gain insight into the common traits of this
594 bacterium. Previous metabolic reconstructions of *X. fastidiosa* were strain-specific, including
595 the model for *X. fastidiosa* subsp. *multiplex* CFBP 8418 (Gerlin et al., 2020) and the model for
596 *X. fastidiosa* subsp. *pauca* De Donno (Oliveira et al., 2023). In the first study, genome
597 comparisons were performed with the strains *X. fastidiosa* subsp. *pauca* 9a5c and subsp.
598 *fastidiosa* Temecula1, suggesting that the results could be extrapolated to these subspecies.
599 In contrast, our reconstruction explicitly incorporates these strains within a broader
600 pangenome framework, providing a more robust representation of the conserved metabolic
601 potential of *X. fastidiosa*.

602 Moreover, the Xfcore metabolic model and the pangenome assembly can serve as a
603 foundation for the reconstruction of strain-specific models, following the protocol described in
604 Norsigian et al. (2020). This framework highlights how the availability of a curated base model
605 can significantly reduce the effort required for the generation of multi-strain metabolic models.
606 Such approaches have already been successfully applied to reconstruct strain-specific models
607 for the *Lactobacillaceae* family and for *Aspergillus fumigatus* species (Mirhakkak et al., 2023;
608 Ardalani et al., 2024). Additionally, our reconstructed model incorporates the ortholog group
609 associated with each gene in the network annotation, enabling the extraction of strain-specific
610 genetic information when required.

611 The Xfcore metabolic model contains 42 genes annotated as pseudogenes in some of the
612 strains. However, several cases suggest that these annotations may not reflect true gene loss
613 but sequencing mistakes, as some genes appear intact in alternative genome assemblies of
614 the same strain or contain frameshift mutations in homopolymeric regions prone to sequencing
615 errors (Cooley & Wright, 2024). Moreover, some of these genes belong to otherwise complete
616 metabolic pathways, making the loss of a single intermediate reaction metabolically unlikely.
617 For these reasons, pseudogene annotations were carefully evaluated during model curation.

618 Some peculiarities were identified when analyzing the characteristics of the metabolic network.
619 For instance, early studies on *X. fastidiosa* metabolism reported the absence of fructose-1,6-
620 bisphosphatase (FBPase) activity and suggested that gluconeogenesis could not occur in this
621 bacterium (Facincani et al., 2003). Consistent with these observations, no FBPase was found
622 in the pangenome. However, gluconeogenesis could be supported by a reversible
623 pyrophosphate-dependent phosphofructokinase (EC 2.7.1.90), which is encoded in the core
624 genome.

625 In addition, the bacterium appears to have a limited set of reactions for reducing power
626 production, as both 6-phosphogluconate dehydrogenase and transhydrogenase are absent
627 from the Xfcore network. In minimal medium with glutamine, pyruvate can be generated
628 through the malic enzyme, which contributes to NADPH production and represents the main
629 connection between the TCA cycle and gluconeogenesis. We did not find any evidence for
630 reactions directly linking pyruvate or phosphoenolpyruvate with the TCA cycle. Therefore, *X.*
631 *fastidiosa* appears to lack typical anaplerotic reactions to replenish the cycle, suggesting that
632 its metabolism operates under relatively constrained network configurations, fully dependent
633 of the environmental supply of precursors of the cycle intermediates, such as the amino acids
634 glutamine or glutamate present in the xylem. Consistent with this observation, simulations in
635 the Xfcore model indicate that growth on hexoses or pentoses, or acetate, requires the
636 presence of a TCA cycle intermediate to initiate the cycle. In the absence of such
637 intermediates, the model cannot sustain growth, reflecting that limited capacity to replenish
638 TCA metabolites. In previous reconstructions, different assumptions allowed growth under
639 these conditions: in the model by Gerlin et al. (2020), growth was supported by the baseless
640 inclusion of the glyoxylate cycle, whereas in the reconstruction by Oliveira et al. (2023) growth
641 was enabled by allowing the malic enzyme to operate reversibly, effectively generating malate
642 from pyruvate. When the malic enzyme is constrained to operate in the
643 oxidative/decarboxylative direction, growth decreases and requires the presence of a TCA
644 intermediate.

645 The phenotypic characterization performed in this work provides a robust dataset, including
646 four independent experiments and five strains belonging to the three main *X. fastidiosa*
647 subspecies (*fastidiosa*, *multiplex* and *pauca*). Previous studies have reported Biolog results
648 for *X. fastidiosa*, such as the work of Gerlin et al. (2020), although in that case the analysis
649 was limited to the strain CFBP8418 (subsp. *multiplex*) used for metabolic modelling. For
650 sugars, the in silico simulations indicated that the Entner–Doudoroff (ED) pathway represents
651 the main glycolytic route through which the metabolic network can metabolize these
652 compounds. This result is consistent with the model proposed by Oliveira et al. (2023), which
653 reached the same conclusion and suggested that this could help protect the bacterium against
654 reactive oxygen species (ROS) generated by the plant defense system (Wang et al., 2017).
655 As previously reported in *P. putida*, the metabolism through the ED pathway has been
656 associated with increased tolerance to oxidative stress due to enhanced NADPH generation
657 (Chavarría et al., 2013).

658 In axenic cultures, *X. fastidiosa* can grow with acetate as a sole carbon source. Remarkably,
659 acetate is a major organic acid present in olive xylem sap (Anguita-Maeso et al., 2021).
660 Intriguingly, GEMs for this organism lack any canonical pathway for acetate assimilation, and
661 previous metabolic reconstructions have addressed this issue using different strategies. In the
662 Xfm1158 model (Gerlin et al., 2020), growth on acetate was enabled by incorporating the
663 glyoxylate cycle, despite the absence of genomic evidence supporting the presence of its key
664 enzymes. In contrast, the iMS50 model (Oliveira et al., 2023), adopted a more conservative
665 position and did not include the glyoxylate cycle, resulting in the inability to simulate growth on
666 acetate. In our reconstruction, the Xfcore model suggested a previously undescribed
667 metabolic solution for growth on acetate. In brief, we propose the first part of the 3HP bi-cycle
668 –an autotrophic pathway described in *Chloroflexus auranticus* by Herter et al. (2002)
669 (Supplementary Figure S8, panel A)–combined with the conversion of propionyl CoA into a
670 biomass precursor. The assimilation of propionyl CoA in *X. fastidiosa* would use a pathway
671 different to the one proposed by Zarzycki and Fuchs (2011) for the co-assimilation of acetate
672 in *C. auranticus* (Supplementary Figure S8, panel B). Thus, in the Xfcore model propionyl CoA
673 can be assimilated into pyruvate through the methylcitrate pathway firstly described in yeasts
674 by Tabuchi et al. (1974) and which is also operative in bacteria like *E. coli* grown in propionate
675 (Brock et al., 2002) (Supplementary Figure S8, panel C).

676 We can compare this new pathway for acetate assimilation with the ones previously described
677 in the literature (Supplementary Table S6). The putative acetate assimilation pathway in *X.*
678 *fastidiosa* (Xf pathway) represents a slight variation of the 3HP pathway described in *C.*
679 *auranticus*, in terms of energy balance and carbon efficiency; in both cases, there is a net gain

680 of carbon. The main difference is that the Xf pathway involves two more enzymatic steps than
681 the half 3HP bi-cycle. Both pathways are more demanding of reducing power than the rest of
682 known routes and, as discussed before, this may explain the increased flux through the TCA
683 cycle in Xfcore under acetate conditions. It is remarkable that *X. fastidiosa* harbors two
684 structurally different IDH isoenzymes, specific for NAD+ or NADP+, respectively (Lv et al.,
685 2018). Interestingly, the evolutionary origin of a NADP-dependent IDH has been correlated
686 with an increased demand of reducing power associated with the use of acetate as carbon
687 source (Zhu et al., 2005). Comparing all the pathways, the shortest solutions are represented
688 by the anaerobic assimilation of acetate by ferredoxin-dependent pyruvate synthase and the
689 widely distributed glyoxylate cycle (Supplementary Table S6).

690 Our proposal of a combination of part of the 3HP bi-cycle with the methylcitrate pathway to
691 explain acetate assimilation by *X. fastidiosa* highlights the role of functional modularity in
692 metabolic adaptation and evolution. Metabolic modules can reorganize or combine to explore
693 biochemical diversity (Schada von Borzyskowski et al., 2020). Functional degeneracy
694 between diverse metabolic solutions also can reflect different dynamics of adaptation to
695 environmental challenges, as described for *Paracoccus denitrificans* (Kremer et al., 2019). On
696 the other hand, in our hypothetical solution for acetate assimilation in *X. fastidiosa* we have
697 proposed several steps catalyzed by enzymes with relaxed substrate specificity. Thus,
698 referring to the pathway in Fig. 3, an acyl-CoA synthetase operates in steps 1 and 5, citrate
699 synthase is also operative as methylcitrate synthase (step 8), and finally aconitase AcnD will
700 act in step 10. Those cases would represent additional examples of the well known metabolic
701 economy observed in symbionts (either pathogens or mutualists) and sustained through
702 reactions operated by promiscuous or multifunctional enzymes (Yus et al., 2009; Kim et al.,
703 2010; Gil & Peretó, 2015). Gerlin et al. (2020) have correlated the lack of enzymatic
704 redundancy in the *X. fastidiosa* metabolic network with a reduced robustness and the
705 characteristic fastidious growth. In any case, we are aware that our in silico hypothesis
706 requires experimental validation, through omics approaches, biochemical characterization of
707 enzyme activities, and ^{13}C-fluxomics experiments. Furthermore, phylogenetic analysis of the
708 involved enzymes also could shed light on the origin and evolutionary tinkering of the pathway,
709 as well as its distribution in the tree of life.

710 Our results revealed some discrepancies between in vitro phenotyping, published
711 observations, and model predictions. Consistent growth on glutamine or glutamate was not
712 detected in the Biolog PM assays for the strains analyzed, whereas growth was sustained in
713 silico. However, glutamine was selected as the main carbon source for the minimal media
714 experiments and simulations because its utilization has been widely reported in the literature

715 for *X. fastidiosa* (Almeida et al., 2004; de Macedo Lemos et al., 2003; Gerlin et al., 2020). In
716 addition, in the minimal media experiments performed in this work, glutamine sustained both
717 bacterial growth and biofilm formation. As per the same reason, glutamic acid was used in the
718 phenotypic simulations because it provided a direct entry point into the TCA cycle,
719 representing a known nitrogen source present in xylem sap (Surano et al., 2024). This
720 glutamate supplementation was consistent with the medium composition used in the Biolog
721 phenotypic assays (available via manufacturer). Moreover, its assimilation is consistent with
722 the predictions of the Xfcore model, which requires substrates capable of replenishing TCA
723 cycle intermediates.

724 Some carbohydrates and derivatives, as well as some organic acids, supported growth in vitro
725 but not in silico, suggesting that certain metabolites and metabolic reactions may be missing
726 from the model, possibly because the corresponding genes are not present in all strains of the
727 pangenome. In the case of lipid substrates, in silico validation could not be performed because
728 the β-oxidation pathway has not been described in *X. fastidiosa*. However, growth on lipid
729 derivatives has been previously reported (Gerlin et al., 2020), suggesting that some
730 alternative, yet undescribed, metabolic pathways may exist. As shown for acetate assimilation,
731 the metabolic model may help guide the search for such alternative pathways by identifying
732 potential metabolic gaps.

733 Finally, several compounds commonly present in xylem sap were also evaluated. Although no
734 growth was detected in vitro for some of them (D-glucose, citrate, L-aspartate and L-alanine),
735 the metabolic model predicted that these substrates could theoretically support growth. These
736 discrepancies may be explained by differences in experimental conditions. In this work, growth
737 was evaluated using OD_{600} measurements, whereas Biolog PM assays typically rely on
738 respiration-based detection. Additionally, factors such as substrate concentration, medium
739 composition, or transport limitations may influence the ability of cells to utilize certain
740 compounds in vitro. For instance, a low initial cell density could limit the activity of the
741 glutamate transporter, preventing the flux required to sustain growth, unlike other carbon
742 sources such as pyruvate. Moreover, in xylem sap *X. fastidiosa* is likely exposed to
743 combinations of carbon sources, which could compensate for metabolic limitations that are
744 not captured when substrates are tested individually in Biolog PM assays.

745 Metabolic reconstructions have been previously used to design minimal growth media for
746 fastidious microorganisms. A notable example is the work for *Mycoplasma pneumoniae* to
747 define a synthetic minimal medium (Yus et al., 2009). This strategy of reverse ecology
748 implicitly validates that genomic information and reconstructed networks can guide the

749 formulation of culture media for other fastidious or uncultured bacteria (Cross et al., 2019;
750 Lewis et al., 2021). Under strictly defined conditions, the use of sugars or other substrates that
751 do not directly feed the TCA cycle would theoretically require the addition of a TCA
752 intermediate. However, in empirical in vitro conditions, intracellular metabolite pools may
753 partially compensate for this requirement, as cells are not metabolically empty at the beginning
754 of the experiment. In natural environments, on the other hand, the chemical diversity
755 accessible to the bacterium would compensate for this metabolic obstacle. Interestingly,
756 although none of the minimal medium tested here supported higher growth, with few
757 exceptions, than the control medium, biofilm formation was observed at comparable levels
758 under these restricted conditions. *X. fastidiosa* is known to colonize xylem vessels primarily in
759 the form of biofilms, which play a key role in its pathogenicity (Marques et al., 2002). This
760 approach aimed to explore whether minimal environmental conditions, such as in the xylem
761 sap, could trigger biofilm development independently of optimal planktonic growth, which was
762 confirmed with the results shown.

763 Another important trait explored in this work was polyamine production in *X. fastidiosa*.
764 Polyamines are well-established modulators of biofilm formation and adhesion in many
765 bacterial pathogens. They influence biofilm development through effects on gene regulation,
766 signaling pathways, and extracellular matrix production. However, there was currently no
767 direct experimental evidence that polyamines are produced by *X. fastidiosa*, modulate its
768 biofilm formation or adhesion. A previous study analyzing nitrogen metabolism in citrus trees
769 infected with *X. fastidiosa* reported high levels of putrescine exclusively in infected plants
770 (Purcino et al., 2007), although this observation was interpreted as associated with plant
771 production, as polyamines are also known to be produced by plants as part of their stress
772 signalling responses (Blázquez, 2024). In other phytopathogens, such as *R. solanacearum*
773 and *P. syringae* polyamine production has been described as a virulence factor (Lowe-Power
774 et al., 2018; Solmi et al., 2025), but this trait has not yet been characterized in *X. fastidiosa*. In
775 these pathogens, polyamines have been proposed to protect bacteria against oxidative stress
776 generated by plant defense responses and may contribute to symptom development during
777 infection.

778 Metabolic modelling has previously been used to explore production of virulence-associated
779 processes in plant pathogens. Other reconstructions of *X. fastidiosa* metabolism (Gerlin et al.,
780 2020; Oliveira et al., 2023) have considered the secretion of two known virulence factors: the
781 LesA protein (Nascimento et al., 2016) and exopolysaccharides (EPS) (da Silva et al., 2001).
782 The metabolic model of the phytopathogen *R. solanacearum* (Peyraud et al., 2016), also
783 incorporated polyamine secretion due to its experimental confirmation. We extended this

concept by exploring the relationship between polyamine production and the virulence-associated factors in *X. fastidiosa*, including the secretion of the LesA protein and exopolysaccharides (EPS).

In this work, both metabolic modelling and experimental analyses indicated that *X. fastidiosa* is capable of producing and secreting polyamines. Metabolic simulations revealed a clear trade-off between biomass production, polyamine biosynthesis, and other known virulence factors, suggesting that the synthesis of these compounds may occur at a metabolic cost for the bacterium. Differences in the maximum achievable fluxes for the three polyamines at minimum biomass levels reflect their distinct biosynthetic costs and precursor requirements within the metabolic network. In particular, spermidine and spermine production appear to be metabolically coupled due to their dependence on shared precursors. Additionally, the simulations revealed a clear trade-off between biomass production and the secretion of virulence-related compounds. Interestingly, spermidine and spermine production appeared to be more compatible with the secretion of LesA and EPS across a broader range of similar biomass levels.

Our experimental data, despite the variability typically observed when working with fastidious bacteria in vitro, showed a higher accumulation of spermidine in the culture supernatant. Additionally, polyamine levels tended to be higher in biofilm-associated cell pellets (CP-B) than in planktonic cells, suggesting a link between polyamine production and the biofilm state of this phytopathogen. While polyamines are established regulators of bacterial biofilms–often acting through EPS synthesis or second messenger pathways (Karatan & Michael, 2013)–their role in *X. fastidiosa* remains untested experimentally. All current works for *X. fastidiosa* focus on EPS composition or processing (Janissen et al., 2015; Castro et al., 2023), the role of surface adhesins and pili (Scala et al., 2025), or of DSF-family quorum sensing signals (Horgan et al., 2024), without an explicit link to polyamine metabolism or signaling. Our results open the possibility that polyamine production could represent an additional virulence-related trait in *X. fastidiosa*. Further in vivo studies will be necessary to determine whether the polyamines detected in infected plants originate from bacterial metabolism and to clarify their role during host colonization by this species.

Overall, the Xfcore metabolic model provides a systems-level framework to investigate the metabolism of *X. fastidiosa* and to generate new hypotheses about its physiology and virulence strategies. In future work, this reconstruction could be integrated with plant metabolic models to explore host–pathogen interactions within the xylem environment.

Conclusions

This work presents the first pangenome-based metabolic reconstruction for *X. fastidiosa*, integrating the conserved metabolism across five subspecies of this phytopathogen. After experimental validation, the Xfcore model enabled the prediction of minimal nutritional requirements, which guided the formulation of defined media capable of supporting biofilm formation in vitro. This success served as further implicit validation of the predictive power of the model. Furthermore, the model suggested a previously undescribed metabolic solution for acetate assimilation into biomass precursors. The simulations also predicted the capacity of *X. fastidiosa* to overproduce polyamines, a result that was confirmed experimentally, representing the first in vitro evidence of polyamine production in this pathogen. Beyond these insights, the Xfcore model provides a robust framework for the reconstruction of strain-specific metabolic models and offers a valuable platform for future studies integrating bacterial and plant metabolism to investigate host–pathogen interactions.

Materials and Methods

Genome data preparation and pangenome reconstruction

A total of 18 *X. fastidiosa* strains were considered for the pangenome assembly (Table 1). Complete, chromosomal, whole-genome data was retrieved from the NCBI Genome database (Sayers et al., 2024). For each strain, the associated plasmid sequences, when available, were also inspected using the BlastKOALA annotation server (Kanehisa et al., 2016) and the NCBI annotation. As none of the plasmid-encoded genes were associated with relevant metabolic functions, plasmid sequences were excluded from the pangenome analysis. Coding sequences, excluding those annotated as pseudogenes, were clustered into ortholog groups (OGs) using InParanoid (Remm et al., 2001), applying a minimum of 80% sequence identity and at least 50% pairwise aligned sequence length, using the BLOSUM 80 substitution matrix. Pairwise ortholog clusters generated by InParanoid were merged into multi-strain ortholog groups using QuickParanoid (http://pl.postech.ac.kr/QuickParanoid/). Genes without a best bidirectional hit in any other genome were classified as “unique” while “accessory” genes were defined as those present at least in two strains. Genes belonging to OGs shared across all strains were considered “core”. Core, accessory and unique gene sets were annotated with BlastKOALA automatic annotated server to explore the functional traits.

850 **Metabolic model reconstruction and refinement**

851 For the constraint-based metabolic model reconstruction and analysis (COBRA), established
852 protocols were followed (Thiele & Palsson, 2010; Nogales, 2017). An initial draft reconstruction
853 of the metabolic network was generated based on the core gene set of the *X. fastidiosa* 9a5c
854 strain using the automatic workflow provided by ModelSEED (Overbeek et al., 2005; Henry et
855 al., 2010). In addition, draft reconstructions were generated for all remaining strains to support
856 the manual curation of the core draft model. Curated genome-scale metabolic models of
857 *Escherichia coli* iJO1366 (Orth et al., 2011) obtained from BiGG Models (King et al., 2016),
858 *Xylella fastidiosa* Xfm1158 (Gerlin et al., 2020) and iMS508 (Oliveira et al., 2023) from
859 BioModels (Malik-Sheriff et al., 2020), and *Xanthomonas campestris* pv. *campestris* str. B100
860 (Schatschneider et al., 2013) were used as references during the curation process.

861 Subsequently, the model was iteratively refined to ensure consistency with available
862 physiological and biochemical data. To facilitate thorough curation of the draft reconstruction,
863 reactions, metabolites, and genes were annotated using identifiers from multiple biochemical
864 databases, including KEGG (Kanehisa et al., 2025), MetaCyc (Caspi et al., 2020), BioCyc
865 (Karp et al., 2019) BiGG Models (King et al., 2016), ModelSEED (Overbeek et al., 2005; Henry
866 et al., 2010), and NCBI databases. SBOannotator (Leonidou et al., 2023) was used to assign
867 SBO terms. BioCyc (Karp et al., 2019), KEGG (Kanehisa et al., 2025), BRENDA (Chang et
868 al., 2021) and Pfam databases (Mistry et al., 2021) were consulted to support manual curation.
869 Consistency analysis of the topological network was conducted to identify gap metabolites
870 and blocked reactions (Ponce-de-Leon et al., 2015). During this step, reaction stoichiometries
871 were revised, including mass and charge balances, reaction directionality and cofactor usage.
872 Similarity-based searches were used to infer missing functions in the model to sequences
873 from the *X. fastidiosa* pangenome, based on sequence and functional homology with other
874 organisms. These analyses were performed using BLASTp (Camacho et al., 2009) and
875 HMMER (Mistry et al., 2013) toolboxes against local sequence databases built from the *X.*
876 *fastidiosa* pangenome whole-genome sequences. Within the HMMER framework, hmmscan
877 and hmmsearch and pfamscan (Madeira et al., 2024) were used to identify conserved protein
878 domains and domain architectures, providing additional support for functional inference based
879 on profile hidden Markov models. Although all pseudogenes were initially excluded from the
880 pangenome analysis–defined as genes predicted to have lost functionality due to frameshift
881 mutations, partial or incomplete sequences, internal codon stops or a high proportion of
882 ambiguous nucleotides–this criterion was later revised in order to avoid overlooking any
883 essential metabolic activity, during the manual model curation. To that end, every missing
884 function was also searched within the accessory gene sets. Accessory functions that were

885 found in the majority of strains and pseudogenized only in a limited number of strains, typically
886 due to point mutations visualized with the MEGAX software (Kumar et al., 2018), were treated
887 as core functions to better represent the general metabolic phenotype of the species (Table
888 S1). Reactions were assigned a confidence score ranging from 0 to 4 according to the level
889 of supporting evidence, following the criteria defined by Thiele and Palsson (2010). Curation
890 efforts focused on pathways central to the conserved physiology of *X. fastidiosa*, including
891 central carbon metabolism, complete biosynthetic routes for amino acids, lipid and nucleotide
892 metabolism, energy metabolism, and selected transport systems (Simpson et al., 2000;
893 Meidanis et al., 2002). In addition, pathways related to redox balance, cofactor biosynthesis
894 and host-associated growth were carefully curated. These included quinone and shikimate
895 biosynthesis, polyamine metabolism, the S-adenosylmethionine (SAM) cycle, sulfur and
896 nitrogen metabolism, and the methionine salvage pathway. Vitamin and cofactor biosynthetic
897 pathways were curated in detail, encompassing pantothenate, folate, riboflavin, thiamine, and
898 porphyrin metabolism. Finally, pathways associated with cell envelope biogenesis and host
899 interaction were refined. This included the biosynthesis of exopolysaccharides (EPS) and
900 lipopolysaccharides (LPS), as well as other fatty acid metabolism. Furthermore, the
901 biosynthesis and export reactions of the LesA protein were incorporated to the model,
902 following previous strain-specific metabolic reconstructions (Gerlin et al., 2020; Oliveira et al.,
903 2023).

904 In parallel with the rest of the network, the biomass reaction was also curated. The biomass
905 reaction generated by ModelSEED was used as a template. Comparison of the biomass
906 reactions of the reference models and the pangenome core one was done. The suitability of
907 each metabolite in the template and potential biomass components were evaluated, including
908 the molar contribution of each one, based on biochemical data and the biomass reactions from
909 the reference models.

910 Manipulation of metabolic reconstructions was carried out with the COBRApy library in Python
911 (Ebrahim et al., 2013). NetworkX v2.4 (Hagberg et al., 2008), Escher v1.7.3 (King et al., 2015),
912 yED Graph Editor v3.18.2 (yWorks GmbH, 2020) and Cytoscape v3.7.1 (Shannon et al., 2003)
913 were used for metabolic network visualization during the curation process. The quality of the
914 final model was evaluated using the MEMOTE v.0.13.0 tool (Lieven et al., 2020). The final
915 GEM is provided in JSON, MAT-File and Systems Biology Markup Language (SBML) formats
916 (Supplementary Material S1).

917

In silico constraints and growth conditions

For reversible reactions, upper and lower bounds of 1000 and -1000 mmol·gDW^{-1}·h^{-1}, were respectively applied. For irreversible reactions, the lower bound–or in specific cases, the upper bound–was fixed at 0 mmol·gDW^{-1}·h^{-1}. Maximization of growth rate was set as the objective function. Oxygen exchange was left unconstrained. The growth-associated maintenance energy (GAM) was fixed at 50.12 mmol·gDW^{-1}·h^{-1}, while the non-growth-associated maintenance energy (NGAM) was set to 3.073 mmol·gDW^{-1}·h^{-1}, according to Gerlin et al. (2020).

For simulation of growth conditions, the lower bounds of exchange reactions were set to zero except for the inorganic ions included in the predicted minimal medium.

For minimal medium simulations, glutamine uptake flux was constrained to -7.25 mmol gDW^{-1} h^{-1} as the carbon and nitrogen source, based on environmental, biochemical and previous metabolic modeling data (Davis, 1992; Gerlin et al., 2020; Orth et al., 2011). For trade-off simulations, glutamine uptake was fixed at -15.665 mmol gDW^{-1} h^{-1} (see *Polyamine and virulence factor trade-off Prediction section* in Materials and Methods).

To evaluate phenotypic substrate utilization data in silico*,* including acetate growth conditions, carbon substrate uptakes were normalized by the number of carbon per molecule, ensuring an equivalent maximum carbon availability across metabolites. A carbon uptake rate of 100 C-mmol·gDW^{-1}·h^{-1} was imposed, following the methodology of Gerlin and coworkers (2020). Ammonia uptake was left unconstrained as the nitrogen source. Additionally, L-glutamate uptake was set to -6 mmol gDW^{-1} h^{-1} to evaluate differences in growth between substrates without limitations imposed by ammonium uptake and anaplerotic reactions of the network.

The complete set of exchange flux constraints in each simulation is provided in Table S5.

Flux Balance and Flux Variability Analyses

Flux Balance Analysis (FBA) and parsimonious Flux Balance Analysis (pFBA) were performed using the COBRApy software (Ebrahim et al., 2013). The optimization problems were solved with the GNU Linear Programming Kit (GLPK) v.5.0 or the IBM ILOG CPLEX Optimizer v.22.1.1. FBA and pFBA were used to compute the maximum value of the objective function and the corresponding flux distribution (Orth et al., 2010; Thiele & Palsson, 2010). Maximization of the growth rate was set as the default cellular objective function. For modelling

949 and simulating growth specific conditions, bounds of some reactions were modified as
950 previously specified in the *In silico constraints and growth conditions* section.

951

952 **Design of synthetic defined minimal media**

953 To design a model-driven minimal medium sustaining the FBA-predicted growth rate under a
954 fixed L-glutamine uptake constraint (7.25 mmol·gDW^{-1}·h^{-1}), the number of active exchange
955 reactions was minimized. This was formulated as a mixed-integer linear programming (MILP)
956 problem and solved using the GLPK solver (Free Software Foundation, 2018), employing the
957 *minimal_medium* implementation from the COBRApy medium module (Ebrahim et al., 2013).
958 Based on the predicted metabolite requirements, six synthetic defined minimal media were
959 designed (mXC1-mXC6, Table S3). The initial formulations (mXC1 and mXC2) were derived
960 from the in silico minimal medium, using glutamine as carbon and nitrogen source, and
961 different iron sources. Concentrations of all components were adapted from existing media
962 known to support *X. fastidiosa* growth. Concentrations of glutamine, hemin chloride and
963 inorganic salts were adapted from PW synthetic medium (Davis et al., 1981), while ferric
964 pyrophosphate concentrations were derived from BCYE (Wells et al., 1981) and 3G10R media
965 (Leite et al., 2004). For subsequent formulations (mXC3 to mXC6), glutamine was replaced
966 with equivalent quantities of alternative carbon sources (sodium acetate or ribose),
967 supplementing with nitrogen sources. Generally, ammonium sulfate was used as an inorganic
968 nitrogen source, whereas cysteine was used as an alternative nitrogen source in mXC6
969 formulation. To validate the biotin-related predictions under growth on acetate, mXC4 medium
970 was supplemented with biotin. Concentration of $(NH_4)_2SO_4$ was obtained from XVM2
971 (*Xanthomonas* apoplast medium) medium (Hiery et al., 2013), cysteine from BCYE and XF-
972 26 (Chang, 1993), and biotin from SXM (Xylem fluid medium) (Neumann, 2003). All media
973 were adjusted to a pH of 6.9 and brought to a final volume of 1 L with sterile distilled water.
974 PD3 broth (Davis et al., 1981) was used as a positive growth control.

975

976 **Acetate assimilation pathways research**

977 To investigate the metabolic strategy employed by *X. fastidiosa* for the conversion of acetate
978 into biomass, the diverse metabolic assimilation pathways described in the literature were
979 searched against the *X. fastidiosa* genome. Reference protein sequences corresponding to
980 the enzymatic steps involved in each pathway were retrieved from the BRENDA database
981 based on their associated EC numbers. Reciprocal BLASTP (v2.9.0+) (Camacho et al., 2009)

982 searches were conducted between these reference sequences and the annotated amino acid
983 sequences of *X. fastidiosa*. Substantial outcomes were obtained by setting specific filtering
984 parameters (coverage greater than 80 %, e-value ≤ 1e−6). Additionally, hmmscan, hmmsearch
985 and pfamscan (Madeira et al., 2024) were used to identify conserved protein domains and
986 domain architectures, providing additional support for functional inference. Finally, the results
987 were manually revised and some selected candidates and enzymatic activities were reviewed
988 using the UniProt database (UniProt Consortium, 2025) to validate results.

989

990 **Polyamine and virulence factors trade-off prediction**

991 Polyamine biosynthesis and degradation pathways were manually curated and revised as
992 described in the metabolic reconstruction section. Special attention was paid to S-
993 adenosylmethionine (SAM) regeneration and the L-methionine salvage pathway. As no
994 experimentally validated polyamine export mechanism has been described in *X. fastidiosa*,
995 demand reactions for putrescine, spermidine, and spermine were incorporated to simulate
996 intracellular production and secretion potential.

997 To investigate potential trade-offs between biomass production, polyamine secretion and
998 virulence factors synthesis (EPS and LesA protein), a two-step optimization strategy was
999 applied. First, an experimental-like scenario was reproduced constraining biomass production
1000 (0.1608 h^{-1}), EPS biosynthesis (1.296 mmol gDW^{-1} h^{-1}) and LesA production (0.0024 mmol
1001 gDW^{-1} h^{-1}) as described in Gerlin et al. (2020). Under these constraints, glutamine uptake was
1002 minimized, resulting in a flux of -15.665 mmol gDW^{-1} h^{-1}. This value was used as the carbon
1003 and nitrogen source uptake for all trade-off simulations. In the second step, biomass was
1004 constrained to a minimum of 0.1608 h^{-1}, and the feasible production space of three target
1005 metabolites was explored. For each metabolic product, the maximum achievable flux at the
1006 minimum fixed biomass level was determined by FBA by maximizing the corresponding
1007 demand or export reaction. Uniform grids (30 intervals per axis) ranging from zero to the
1008 maximum achievable flux were generated for each metabolite. For every combination of target
1009 fluxes (p1, p2, p3), biomass was constrained to a minimum value of 0.1608 h^{-1} and the model
1010 was re-optimized maximizing the growth rate as the objective function using the CPLEX
1011 Optimizer. Only feasible solutions were retained. This sampling enabled the reconstruction of
1012 two-dimensional phase planes approximating the surface of the Pareto front, representing the
1013 trade-off between metabolite production and biomass growth rate. Phase planes were
1014 obtained by fixing one product to zero and projecting the feasible region of the remaining two

1015 metabolites. The resulting solution space was visualized using tricontour and tricontourf
1016 functions from the Matplotlib library. Biomass flux was represented as a continuous color
1017 gradient.

1018

1019 **Bacterial strains and culture conditions**

1020 Seven *X. fastidiosa* strains used in the in vitro studies including two from subspecies *fastidiosa*
1021 isolated from grapevine in California (Temecula1) and Balearic island (IVIA5770), three from
1022 subspecies *multiplex* isolated from almond trees in Alicante (Spain) (ESVL and IVIA5901) and
1023 wild olive in Balearic island (XYL468) and two from subspecies *pauca* isolated from olive trees
1024 (De Donno and XYL1961/18) in Apulia (Italy) and Ibiza (Spain), respectively. Stocks of *X.*
1025 *fastidiosa* strains were stored in phosphate buffered saline (PBS) plus 50 % glycerol at -80
1026 °C. For all the experiments, strains were recovered from glycerol stocks on plates of PD3
1027 (Davis et al., 1981) or BCYE (Wells et al., 1981) media incubated at 28 °C in the dark. After 6
1028 to 8 days, cells were re-streaked onto new plates and cultured for 5 to 7 days before using
1029 them in each experiment.

1030

1031 **Phenotypic characterization of *Xylella fastidiosa* strains**

1032 Phenotypic characterization of five *X. fastidiosa* strains (ESVL, De Donno, IVIA5901,
1033 Temecula1, and XYL1961/18) was performed using the Biolog phenotype microarray (PM)
1034 system (Biolog, Hayward, California). The potential utilization of 190 carbon sources was
1035 determined using the PM1 and PM2 plates. For PM plate inoculation, bacterial cells were
1036 scraped from solid culture plates and resuspended in the IF-0a GN/GP base inoculating fluid
1037 (Biolog, Hayward, California) and the bacterial suspension was mixed with the corresponding
1038 additive solutions for each PM plate and the Dye Mix G, to reach a final optical density at 600
1039 nm (OD_{600}) of 0.08 according to the manufacturer's protocol. Subsequently, 100 µL of a cell
1040 suspension of each *X. fastidiosa* strain was added to each well of the PM microplates and
1041 incubated at 28 °C during 9 days without agitation. Bacterial growth was assessed by
1042 measuring OD_{600} using a microplate absorbance reader i-Mark TM spectrophotometer (Bio-
1043 Rad, Hercules, CA, USA). Four independent experiments were conducted for each strain and
1044 PM substrate-type microplate.

1045

1046 **Growth of *Xylella fastidiosa* strains in designed synthetic defined minimal**
1047 **media**

1048 In vitro culture experiments using the six minimal media (Table S3) were conducted with seven
1049 *X. fastidiosa* strains (ESVL, De Donno, IVIA5770, IVIA5901, Temecula1, XYL1961/18, and
1050 XYL468) as described by Román-Écija and coworkers (2023) to assess the ability of the
1051 designed minimal media to support total and planktonic growth, as well as biofilm formation of
1052 the seven *X. fastidiosa* strains. Briefly, a cell suspension of each strain was diluted in each
1053 minimal medium to reach at OD_{600} = 0.08. Cell suspensions (200 µL) were inoculated in
1054 polystyrene 96-well microplates (Sarstedt, Nümbrecht, Germany) and incubated at 28 °C
1055 during 7 days without agitation. At least four independent experiments were conducted, and
1056 each experiment included 5 replicated wells per treatment. Non-inoculated medium served as
1057 negative control. Bacterial growth was measured daily by measuring OD_{600}. After the 7-day
1058 incubation, planktonic growth was assessed by transferring 150 µL cell suspension to a new
1059 plate and measuring the OD_{600}. Biofilm formation was estimated using the crystal violet assay
1060 as described (Román-Écija et al. 2023).

1061

1062 **Polyamines production by *Xylella fastidiosa* strains in liquid medium**

1063 To validate the metabolic model predictions for the ability of *X. fastidiosa* to produce
1064 polyamines (putrescine, spermidine and spermine) during in vitro culture two experiments
1065 were performed. An initial experiment was carried out to determine the production of
1066 polyamines by *X. fastidiosa* during *in vitro* culture. For that, 10-mL cell suspensions at OD_{600}
1067 = 0.05 of six *X. fastidiosa* strains (ESVL, De Donno, IVIA5770, Temecula1, XYL1961/18 and
1068 XYL468) were used to inoculate 50-mL glass flasks and incubated under agitation at 28 °C.
1069 After 9 days of growth, two types of samples were collected for polyamines extraction. One
1070 type of sample included *X. fastidiosa* cells from planktonic growth plus those present in the
1071 biofilms formed on the glass surface at the air-liquid interface. For that, cells were scratched
1072 from the attachment ring formed on the glass wall and vortexed. Then, the bacterial cell pellet
1073 (CP) was obtained after centrifugation at 14,000 rpm for 10 min of the entire culture. The
1074 second type of sample included the culture supernatant (SP). At least two biological replicates
1075 for each strain were performed. In the second experiment, three *X. fastidiosa* strains were
1076 used (ESVL, De Donno and Temecula1 strains). In this experiment, three types of samples
1077 were obtained after 5 and 12 days of growth. For each strain and sampling point, culture cells
1078 in planktonic growth were collected by transferring the entire culture to a new falcon tube.
1079 Then, a cell pellet from planktonic growth (CP-P) and a supernatant (SP) were obtained after

1080 centrifugation as described above. To collect cells growing in biofilms, the biofilm formed on
1081 the glass surface was scraped with a loop and resuspended with a pipette using 1 mL of sterile
1082 distilled water. Then, a cell pellet from biofilms (CP-B) was collected by the centrifugation and
1083 removal of the supernatant. In this second experiment, four biological replicates for each strain
1084 and condition were obtained.

1085 The polyamine extraction and quantification of the bacterial cell pellets (CP-P and CP-B) and
1086 supernatant (SP) samples were carried out according to Solé-Gil and coworkers (2019) with
1087 small modifications. Briefly, bacterial cell pellets were resuspended in 1 mL sterile water,
1088 treated with lysozyme (10 $mg \cdot mL^{-1}$), and kept on ice for 10 minutes. Subsequently, bacterial
1089 cells were disrupted by sonication (10 cycles of 30 seconds each). After centrifugation at
1090 10,000 rpm for 10 min, 500 µL of the supernatants were treated with 2.5 mL of perchloric acid
1091 5 % (w/v). Culture supernatants (2.5 mL) were also treated with 2.5 mL of perchloric acid. At
1092 this point, pre-treated samples were stored at -20 °C and sent for analysis of presence of
1093 polyamines at the Metabolomics Service of the Institute of Molecular and Cellular Biology of
1094 Plants (IBMCP, Valencia). Before analysis, 500 µL of the internal standard (1, 6-
1095 Hexanediamine 1 mM, HD) were added to each sample. Polyamines were quantified by HPLC
1096 analysis as described by Santos and coworkers (2021). Measurements were done in triplicate.

1097

1098 **Data processing and statistical analysis**

1099 Growth curves of the different *X. fastidiosa* strains growing in each PM compound or minimal
1100 media were obtained by accumulating OD_{600} values over time from the date of inoculation. To
1101 evaluate growth in minimal media, the OD_{600} value of the control wells was subtracted from
1102 each time point to obtain the net absorbance. Cumulative growth was then calculated by
1103 subtracting the initial net absorbance at the beginning of the experiment from the net
1104 absorbance on each subsequent day. For both experiments, the standardized area under the
1105 growth progress curve (sAUGPC) was calculated using the trapezoidal integration method
1106 standardized by duration of the experiment in days (Simko & Piepho, 2012).

1107 In the PM study, metabolic assimilation by *X. fastidiosa* was determined by normalizing the
1108 sAUGPC of each compound against the strain- and plate-specific negative control (NC).
1109 Following the criteria of Gerlin and coworkers (2020), a compound was considered as positive
1110 carbon source ('Growth') if its sAUGPC was at least 1.14 times higher than the NC.
1111 Specifically, a normalized sAUGPC was calculated as 100 x [sAUGPC - (1.14 * $sAUGPC_{NC}$)].
1112 Negative values after normalization were set to zero. Growth was categorized based on

consistency: a compound was considered assimilated only if the normalized sAUGPC remained positive in at least three of the four biological replicates. Conversely, it was classified as 'No growth' if assimilation occurred in zero or one replicates; otherwise, growth was assessed to be ‘Undetermined’.

Polyamine concentrations were quantified in both cell pellets (CP-P and CP-B) and supernatants (SP). For SP samples, net polyamine content was calculated by subtracting the mean concentration for each polyamine measured of the non-inoculated negative control medium (PD3). This correction was not applied to the pellet samples, as centrifugation removes the influence of the initial medium. Any negative values after normalization were set to zero.

Statistical analyses and data visualization were conducted using R software. Given the variability of bacterial growth and polyamines production, Wilcoxon rank-sum tests were used for all pairwise comparisons ($P \leq 0.05$). For minimal media and biofilm experiments, each tested medium was compared against the PD3 control, and between media pairs sharing the same carbon source. For polyamine data, differences between time points within each sample type and strain were assessed.

Data were visualized using violin plots for growth and biofilm formation in minimal media, and polyamine data. For polyamine results, a pseudo-logarithmic scale was used to facilitate comparison across several orders of magnitude. To visualize the metabolic profiles across PM plates, two heatmap approaches were used. First, a quantitative heatmap was generated to represent the normalized sAUGPC values, with a pseudo-logarithmic transformation for the color scale. Values of zero (no growth) were set as transparent. Second, discrete heatmaps were obtained to summarize growth categories across the four biological replicates. All visualizations were produced using ggplot2, ggpubr and ggh4x packages in R.

Author contributions

Paola Corbín Agustí: Conceptualization, Methodology, Formal analysis, Visualization, Investigation, Software, Data curation, Writing– Original draft, Reviewing and Editing. **Miguel Álvarez Herrera**: Methodology, Formal analysis, Visualization, Investigation, Software, Writing– Reviewing and editing. **Miguel Román Écija**: Methodology, Formal analysis, Investigation, Writing– Reviewing and editing. **Patricia Álvarez**: Methodology, Investigation, Software, Writing– Reviewing and editing. **Marta Tortajada**: Conceptualization, Writing–

Reviewing and editing. **Juli Peretó**: Conceptualization, Supervision, Funding acquisition, Writing– Original draft, Reviewing and Editing. **Blanca B. Landa**: Conceptualization, Supervision, Funding acquisition, Writing– Original draft, Reviewing and Editing.

Funding

P.C.-A. was recipient of a predoctoral fellowship from the Generalitat Valenciana "Subvenciones para la contratación de personal investigador de carácter predoctoral (ACIF)", with reference ACIF/2021/110. M.Á.-H. was supported by the Generalitat Valenciana and the European Social Fund "ESF Investing in your future" through grant CIACIF/2022/333. J.P. acknowledges the generic support of CYTED (Iber-Xyfas network "Red Iberoamericana para la vigilancia de *Xylella fastidiosa*", ref. 119RT0569) as well as of his host institutions Universitat de València and CSIC. This work was financed by the HORIZON-CL6-2021-FARM2FORK-01 project BeXyl (Beyond *Xylella*, Integrated Management Strategies for Mitigating *Xylella fastidiosa* impact in Europe; Grant ID No 101060593). The funders had no role in study design, data collection and analysis, decision to publish, or presentation of the manuscript.

Conflicts of Interest

M. Tortajada is a former employee of Biopolis-Archer Daniels Midland and contributed to this study in their personal capacity. The authors declare no conflicts of interest.

Data Availability Statement

All relevant data are within the manuscript and its additional supporting information. Detailed supplementary files and the code will be made publicly available upon peer-reviewed publication and are available from the corresponding author on request.

Acknowledgements

The authors thank the expert support of Miguel Ángel Blázquez and Francisco Vera-Sirera (IBMCP, UPV-CSIC) and the IBMCP Metabolomics Facility for the polyamine analyses. The authors thank Gonzalo de Oyanguren for the initial steps into the pangenome analysis. Figures 1C and 3 were created in BioRender. Smith, J. (2025).

References

Almeida, R. P. P., Mann, R., & Purcell, A. H. (2004). *Xylella fastidiosa* cultivation on a minimal solid defined medium. *Current Microbiology*, *48*(5), 368–372. https://doi.org/10.1007/s00284-003-4219-x

Anguita-Maeso, M., Haro, C., Montes-Borrego, M., Fuente, L. D. L., Navas-Cortés, J. A., & Landa, B. B. (2021). Metabolomic, ionomic and microbial characterization of olive xylem sap reveals differences according to plant age and genotype. *Agronomy*, *11*(6). https://doi.org/10.3390/agronomy11061179

Ardalani, O., Phaneuf, P. V., Mohite, O. S., Nielsen, L. K., & Palsson, B. O. (2024). Pangenome reconstruction of *Lactobacillaceae* metabolism predicts species-specific metabolic traits. *mSystems*, *9*(7), e00156-24. https://doi.org/10.1128/msystems.00156-24

Blázquez, M. A. (2024). Polyamines: their role in plant development and stress. *Annual Review of Plant Biology*, *75*(Volume 75, 2024), 95–117. https://doi.org/10.1146/annurev-arplant-070623-110056

Brämer, C. O., & Steinbüchel, A. (2001). The methylcitric acid pathway in *Ralstonia eutropha*: New genes identified involved in propionate metabolism. *Microbiology*, *147*(8), 2203–2214. https://doi.org/10.1099/00221287-147-8-2203

Brock, M., Maerker, C., Schütz, A., Völker, U., & Buckel, W. (2002). Oxidation of propionate to pyruvate in *Escherichia coli*: Involvement of methylcitrate dehydratase and aconitase. *European Journal of Biochemistry*, *269*(24), 6184–6194. https://doi.org/10.1046/j.1432-1033.2002.03336.x

Camacho, C., Coulouris, G., Avagyan, V., Ma, N., Papadopoulos, J., Bealer, K., & Madden, T. L. (2009). BLAST+: Architecture and applications. *BMC Bioinformatics*, *10*(1), 421. https://doi.org/10.1186/1471-2105-10-421

Campanharo, J. C., Lemos, M. V. F., & Lemos, E. G. de M. (2003). Growth optimization procedures for the phytopathogen *Xylella fastidiosa*. *Current Microbiology*, *46*(2), 0099–0102. https://doi.org/10.1007/s00284-002-3829-z

Caspi, R., Billington, R., Keseler, I. M., Kothari, A., Krummenacker, M., Midford, P. E., Ong, W. K., Paley, S., Subhraveti, P., & Karp, P. D. (2020). The MetaCyc database of metabolic pathways and enzymes—A 2019 update. *Nucleic Acids Research*, *48*(D1), D445–D453. https://doi.org/10.1093/nar/gkz862

Castro, C., Ndukwe, I., Heiss, C., Black, I., Ingel, B. M., Guevara, M., Sun, Y., Azadi, P., Sun, Q., & Roper, M. C. (2023). *Xylella fastidiosa* modulates exopolysaccharide polymer length and the dynamics of biofilm development with a β-1,4-endoglucanase. *mBio*,

14(5), e01395-23. https://doi.org/10.1128/mbio.01395-23

Chang, A., Jeske, L., Ulbrich, S., Hofmann, J., Koblitz, J., Schomburg, I., Neumann-Schaal, M., Jahn, D., & Schomburg, D. (2021). BRENDA, the ELIXIR core data resource in 2021: New developments and updates. *Nucleic Acids Research*, *49*(D1), D498–D508. https://doi.org/10.1093/nar/gkaa1025

Chang, C. J. (1993). *Xylella fastidiosa*: Cultivation in chemically defined medium. *Phytopathology*, *83*(2), 192. https://doi.org/10.1094/Phyto-83-192

Chatterjee, S., Almeida, R. P. P., & Lindow, S. (2008). Living in two worlds: the plant and insect lifestyles of *Xylella fastidiosa. Annual Review of Phytopathology*, *46*(1), 243–271. https://doi.org/10.1146/annurev.phyto.45.062806.094342

Chavarría, M., Nikel, P. I., Pérez-Pantoja, D., & de Lorenzo, V. (2013). The Entner-Doudoroff pathway empowers *Pseudomonas putida* KT2440 with a high tolerance to oxidative stress. *Environmental Microbiology*, *15*(6), 1772–1785. https://doi.org/10.1111/1462-2920.12069

Cooley, N. P., & Wright, E. S. (2024). Many purported pseudogenes in bacterial genomes are bona fide genes. *BMC Genomics*, *25*(1), 365. https://doi.org/10.1186/s12864-024-10137-0

Cross, K. L., Campbell, J. H., Balachandran, M., Campbell, A. G., Cooper, C. J., Griffen, A., Heaton, M., Joshi, S., Klingeman, D., Leys, E., Yang, Z., Parks, J. M., & Podar, M. (2019). Targeted isolation and cultivation of uncultivated bacteria by reverse genomics. *Nature Biotechnology*, *37*(11), 1314–1321. https://doi.org/10.1038/s41587-019-0260-6

da Silva, F. R., Vettore, A. L., Kemper, E. L., Leite, A., & Arruda, P. (2001). Fastidian gum: The *Xylella fastidiosa* exopolysaccharide possibly involved in bacterial pathogenicity. *FEMS Microbiology Letters*, *203*(2), 165–171. https://doi.org/10.1111/j.1574-6968.2001.tb10836.x

Davis, M. J. (1992). Fastidious bacteria of plant vascular tissues and their invertebrate vectors. In *The Prokaryotes* (pp. 4030–4049). *Springer*. https://doi.org/10.1007/978-1-4757-2191-1_66

Davis, M. J., French, W. J., & Schaad, N. W. (1981). Axenic culture of the bacteria associated with phony disease of peach and plum leaf scald. *Current Microbiology*, *6*(5), 309–314. https://doi.org/10.1007/BF01566883

Davis, M. J., Gillaspie, A. G., Harris, R. W., & Lawson, R. H. (1980). Ratoon Stunting Disease of Sugarcane: Isolation of the Causal Bacterium. *Science*, *210*(4476), 1365–1367. https://doi.org/10.1126/science.210.4476.1365

De La Fuente, L., Navas-Cortés, J. A., & Landa, B. B. (2024). Ten challenges to understanding

and managing the insect-transmitted, xylem-limited bacterial pathogen *Xylella fastidiosa*. *Phytopathology®*, *114*(5), 869–884. https://doi.org/10.1094/PHYTO-12-23-0476-KC

de Macedo Lemos, E. G., Alves, L. M. C., & Campanharo, J. C. (2003). Genomics-based design of defined growth media for the plant pathogen *Xylella fastidiosa*. *FEMS Microbiology Letters*, *219*(1), 39–45. https://doi.org/10.1016/S0378-1097(02)01189-8

Denancé, N., Briand, M., Gaborieau, R., Gaillard, S., & Jacques, M.-A. (2019). Identification of genetic relationships and subspecies signatures in *Xylella fastidiosa*. *BMC Genomics*, *20*(1), 239. https://doi.org/10.1186/s12864-019-5565-9

Dolan, S. K., Wijaya, A., Geddis, S. M., Spring, D. R., Silva-Rocha, R., & Welch, M. (2018). Loving the poison: The methylcitrate cycle and bacterial pathogenesis. *Microbiology*, *164*(3), 251–259. https://doi.org/10.1099/mic.0.000604

Ebrahim, A., Lerman, J. A., Palsson, B. O., & Hyduke, D. R. (2013). COBRApy: COnstraints-Based Reconstruction and Analysis for Python. *BMC Systems Biology*, *7*(1), 74. https://doi.org/10.1186/1752-0509-7-74

EFSA (European Food Safety Authority), E. F. S., Cavalieri, V., Fasanelli, E., Furnari, G., Gibin, D., Gutierrez Linares, A., La Notte, P., Pasinato, L., & Stancanelli, G. (2026). Update of the *Xylella* spp. Host plant database – Systematic literature search up to 30 June 2025. *EFSA Journal*, *24*(1), e9840. https://doi.org/10.2903/j.efsa.2026.9840

Erb, T. J., Berg, I. A., Brecht, V., Müller, M., Fuchs, G., & Alber, B. E. (2007). Synthesis of C_5 -dicarboxylic acids from C_2 -units involving crotonyl-CoA carboxylase/reductase: The ethylmalonyl-CoA pathway. *Proceedings of the National Academy of Sciences*, *104*(25), 10631–10636. https://doi.org/10.1073/pnas.0702791104

Facincani, A. P., Ferro, J. A., Pizauro Jr., J. M., Pereira Jr., H. A., Lemos, E. G. de M., Prado, A. L. do, & Ferro, M. I. T. (2003). Carbohydrate metabolism of *Xylella fastidiosa*: Detection of glycolytic and pentose phosphate pathway enzymes and cloning and expression of the enolase gene. *Genetics and Molecular Biology*, *26*, 203–211. https://doi.org/https://doi.org/10.1590/S1415-47572003000200015

Fausto, C., Araniti, F., Mininni, A. N., Crecchio, C., Scagliola, M., Bleve, G., Dichio, B., & Sofo, A. (2021). Differential olive grove management regulates the levels of primary metabolites in xylem sap. *Plant and Soil*, *460*(1–2), 281–296. https://doi.org/10.1007/s11104-020-04800-0

Garschagen, L. S., Franke, T., & Deppenmeier, U. (2021). An alternative pentose phosphate pathway in human gut bacteria for the degradation of C5 sugars in dietary fibers. *The FEBS Journal*, *288*(6), 1839–1858. https://doi.org/10.1111/febs.15511

Gerlin, L., Cottret, L., Cesbron, S., Taghouti, G., Jacques, M.-A., Genin, S., & Baroukh, C.

(2020). Genome-scale investigation of the metabolic determinants generating bacterial fastidious growth. *mSystems*, *5*(2), 10.1128/msystems.00698-19. https://doi.org/10.1128/msystems.00698-19

Gil, R., & Peretó, J. (2015). Small genomes and the difficulty to define minimal translation and metabolic machineries. *Frontiers in Ecology and Evolution*, *3*. https://doi.org/10.3389/fevo.2015.00123

Gu, C., Kim, G. B., Kim, W. J., Kim, H. U., & Lee, S. Y. (2019). Current status and applications of genome-scale metabolic models. *Genome Biology*, *20*(1), 121. https://doi.org/10.1186/s13059-019-1730-3

Hagberg, A., Swart, P. J., & Schult, D. A. (2008). Exploring network structure, dynamics, and function using NetworkX. In G. Varoquaux, T. Vaught, & J. Millman (Eds.), *Proceedings of the 7th Python in Science Conference (SciPy2008)* (pp. 11–15).

Hanage, W. P., Fraser, C., & Spratt, B. G. (2005). Fuzzy species among recombinogenic bacteria. *BMC Biology*, *3*(1), 6. https://doi.org/10.1186/1741-7007-3-6

Henry, C. S., DeJongh, M., Best, A. A., Frybarger, P. M., Linsay, B., & Stevens, R. L. (2010). High-throughput generation, optimization and analysis of genome-scale metabolic models. *Nature Biotechnology*, *28*(9), 977–982. https://doi.org/10.1038/nbt.1672

Herter, S., Fuchs, G., Bacher, A., & Eisenreich, W. (2002). A bicyclic autotrophic CO2 fixation pathway in *Chloroflexus aurantiacus*. *Journal of Biological Chemistry*, *277*(23), 20277–20283. https://doi.org/10.1074/jbc.M201030200

Hiery, E., Adam, S., Reid, S., Hofmann, J., Sonnewald, S., & Burkovski, A. (2013). Genome-wide transcriptome analysis of *Clavibacter michiganensis* subsp. *michiganensis* grown in xylem mimicking medium. *Journal of Biotechnology*, *168*(4), 348–354. https://doi.org/10.1016/j.jbiotec.2013.09.006

Horgan, C., Baccari, C., O'Driscoll, M., Lindow, S. E., & O'Sullivan, T. P. (2024). BDSF analogues inhibit quorum sensing-regulated biofilm production in *Xylella fastidiosa*. *Microorganisms*, *12*(12), 2496. https://doi.org/10.3390/microorganisms12122496

Ibarra, R. U., Edwards, J. S., & Palsson, B. O. (2002). *Escherichia coli* K-12 undergoes adaptive evolution to achieve in silico predicted optimal growth. *Nature*, *420*(6912), 186–189. https://doi.org/10.1038/nature01149

Igarashi, K., & Kashiwagi, K. (2010). Characteristics of cellular polyamine transport in prokaryotes and eukaryotes. *Plant Physiology and Biochemistry: PPB*, *48*(7), 506–512. https://doi.org/10.1016/j.plaphy.2010.01.017

Janissen, R., Murillo, D. M., Niza, B., Sahoo, P. K., Nobrega, M. M., Cesar, C. L., Temperini, M. L. A., Carvalho, H. F., De Souza, A. A., & Cotta, M. A. (2015). Spatiotemporal distribution of different extracellular polymeric substances and filamentation mediate

Xylella fastidiosa adhesion and biofilm formation. *Scientific Reports*, *5*(1), 9856. https://doi.org/10.1038/srep09856

Jolley, K. A., Bray, J. E., & Maiden, M. C. J. (2018). Open-access bacterial population genomics: BIGSdb software, the PubMLST.org website and their applications. *Wellcome Open Research*, *3*, 124. https://doi.org/10.12688/wellcomeopenres.14826.1

Kanehisa, M., Furumichi, M., Sato, Y., Matsuura, Y., & Ishiguro-Watanabe, M. (2025). KEGG: Biological systems database as a model of the real world. *Nucleic Acids Research*, *53*(D1), D672–D677. https://doi.org/10.1093/nar/gkae909

Kanehisa, M., Sato, Y., & Morishima, K. (2016). BlastKOALA and GhostKOALA: KEGG Tools for functional characterization of genome and metagenome sequences. *Journal of Molecular Biology*, *428*(4), 726–731. https://doi.org/10.1016/j.jmb.2015.11.006

Karatan, E., & Michael, A. J. (2013). A wider role for polyamines in biofilm formation. *Biotechnology Letters*, *35*(11), 1715–1717. https://doi.org/10.1007/s10529-013-1286-3

Karp, P. D., Billington, R., Caspi, R., Fulcher, C. A., Latendresse, M., Kothari, A., Keseler, I. M., Krummenacker, M., Midford, P. E., Ong, Q., Ong, W. K., Paley, S. M., & Subhraveti, P. (2019). The BioCyc collection of microbial genomes and metabolic pathways. *Briefings in Bioinformatics*, *20*(4), 1085–1093. https://doi.org/10.1093/bib/bbx085

Khomyakova, M., Bükmez, Ö., Thomas, L. K., Erb, T. J., & Berg, I. A. (2011). A methylaspartate cycle in Haloarchaea. *Science*, *331*(6015), 334–337. https://doi.org/10.1126/science.1196544

Kim, J., Kershner, J. P., Novikov, Y., Shoemaker, R. K., & Copley, S. D. (2010). Three serendipitous pathways in *E. coli* can bypass a block in pyridoxal-5'-phosphate synthesis. *Molecular Systems Biology*, *6*, 436. https://doi.org/10.1038/msb.2010.88

King, Z. A., Dräger, A., Ebrahim, A., Sonnenschein, N., Lewis, N. E., & Palsson, B. O. (2015). Escher: A web application for building, sharing, and embedding data-rich visualizations of biological pathways. *PLOS Computational Biology*, *11*(8), e1004321. https://doi.org/10.1371/journal.pcbi.1004321

King, Z. A., Lu, J., Dräger, A., Miller, P., Federowicz, S., Lerman, J. A., Ebrahim, A., Palsson, B. O., & Lewis, N. E. (2016). BiGG Models: A platform for integrating, standardizing and sharing genome-scale models. *Nucleic Acids Research*, *44*(D1), D515–D522. https://doi.org/10.1093/nar/gkv1049

Koendjbiharie, J. G., Hon, S., Pabst, M., Hooftman, R., Stevenson, D. M., Cui, J., Amador-Noguez, D., Lynd, L. R., Olson, D. G., & van Kranenburg, R. (2020). The pentose phosphate pathway of cellulolytic clostridia relies on 6-phosphofructokinase instead of transaldolase. *The Journal of Biological Chemistry*, *295*(7), 1867–1878.

https://doi.org/10.1074/jbc.RA119.011239

Kornberg, H. L., & Krebs, H. A. (1957). Synthesis of cell constituents from C2-units by a modified tricarboxylic acid cycle. *Nature*, *179*(4568), 988–991. https://doi.org/10.1038/179988a0

Kremer, K., Van Teeseling, M. C. F., Schada Von Borzyskowski, L., Bernhardsgrütter, I., Van Spanning, R. J. M., Gates, A. J., Remus-Emsermann, M. N. P., Thanbichler, M., & Erb, T. J. (2019). Dynamic metabolic rewiring enables efficient acetyl coenzyme a assimilation in *Paracoccus denitrificans*. *mBio*, *10*(4), e00805-19. https://doi.org/10.1128/mBio.00805-19

Kumar, S., Stecher, G., Li, M., Knyaz, C., & Tamura, K. (2018). MEGA X: Molecular evolutionary genetics analysis across computing platforms. *Molecular Biology and Evolution*, *35*(6), 1547–1549. https://doi.org/10.1093/molbev/msy096

Landa, B. B., Castillo, A. I., Giampetruzzi, A., Kahn, A., Román-Écija, M., Velasco-Amo, M. P., Navas-Cortés, J. A., Marco-Noales, E., Barbé, S., Moralejo, E., Coletta-Filho, H. D., Saldarelli, P., Saponari, M., & Almeida, R. P. P. (2020). Emergence of a plant pathogen in Europe associated with multiple intercontinental introductions. *Applied and Environmental Microbiology*, *86*(3), e01521-19. https://doi.org/10.1128/AEM.01521-19

Landa, B. B., Saponari, M., Feitosa-Junior, O. R., Giampetruzzi, A., Vieira, F. J. D., Mor, E., & Robatzek, S. (2022). *Xylella fastidiosa* 's relationships: The bacterium, the host plants, and the plant microbiome. *New Phytologist*, *234*(5), 1598–1605. https://doi.org/10.1111/nph.18089

Leite, B., Andersen, P. C., & Ishida, M. L. (2004). Colony aggregation and biofilm formation in xylem chemistry-based media for *Xylella fastidiosa*. *FEMS Microbiology Letters*, *230*(2), 283–290. https://doi.org/10.1016/S0378-1097(03)00917-0

Leonidou, N., Fritze, E., Renz, A., & Dräger, A. (2023). SBOannotator: A Python tool for the automated assignment of systems biology ontology terms. *Bioinformatics*, *39*(7). https://doi.org/10.1093/bioinformatics/btad437

Lewis, W. H., Tahon, G., Geesink, P., Sousa, D. Z., & Ettema, T. J. G. (2021). Innovations to culturing the uncultured microbial majority. *Nature Reviews Microbiology*, *19*(4), 225–240. https://doi.org/10.1038/s41579-020-00458-8

Lieven, C., Beber, M. E., Olivier, B. G., Bergmann, F. T., Ataman, M., Babaei, P., Bartell, J. A., Blank, L. M., Chauhan, S., Correia, K., Diener, C., Dräger, A., Ebert, B. E., Edirisinghe, J. N., Faria, J. P., Feist, A. M., Fengos, G., Fleming, R. M. T., García-Jiménez, B., … Zhang, C. (2020). MEMOTE for standardized genome-scale metabolic model testing. *Nature Biotechnology*, *38*(3), 272–276. https://doi.org/10.1038/s41587-

1386 020-0446-y
1387 Lowe-Power, T. M., Hendrich, C. G., Von Roepenack-Lahaye, E., Li, B., Wu, D., Mitra, R.,
1388 Dalsing, B. L., Ricca, P., Naidoo, J., Cook, D., Jancewicz, A., Masson, P., Thomma,
1389 B., Lahaye, T., Michael, A. J., & Allen, C. (2018). Metabolomics of tomato xylem sap
1390 during bacterial wilt reveals *Ralstonia solanacearum* produces abundant putrescine, a
1391 metabolite that accelerates wilt disease. *Environmental Microbiology*, *20*(4), 1330–
1392 1349. https://doi.org/10.1111/1462-2920.14020
1393 Lv, P., Tang, W., Wang, P., Cao, Z., & Zhu, G. (2018). Enzymatic characterization and
1394 functional implication of two structurally different isocitrate dehydrogenases from
1395 *Xylella fastidiosa*. *Biotechnology and Applied Biochemistry*, *65*(2), 230–237.
1396 https://doi.org/10.1002/bab.1560
1397 Madeira, F., Madhusoodanan, N., Lee, J., Eusebi, A., Niewielska, A., Tivey, A. R. N., Lopez,
1398 R., & Butcher, S. (2024). The EMBL-EBI Job Dispatcher sequence analysis tools
1399 framework in 2024. *Nucleic Acids Research*, *52*(W1), W521–W525.
1400 https://doi.org/10.1093/nar/gkae241
1401 Malik-Sheriff, R. S., Glont, M., Nguyen, T. V. N., Tiwari, K., Roberts, M. G., Xavier, A., Vu, M.
1402 T., Men, J., Maire, M., Kananathan, S., Fairbanks, E. L., Meyer, J. P., Arankalle, C.,
1403 Varusai, T. M., Knight-Schrijver, V., Li, L., Dueñas-Roca, C., Dass, G., Keating, S. M.,
1404 … Hermjakob, H. (2020). BioModels—15 years of sharing computational models in life
1405 science. *Nucleic Acids Research*, *48*(D1), D407–D415.
1406 https://doi.org/10.1093/nar/gkz1055
1407 Marques, L. L. R., Ceri, H., Manfio, G. P., Reid, D. M., & Olson, M. E. (2002). Characterization
1408 of biofilm formation by *Xylella fastidiosa* in vitro. *Plant Disease*, *86*(6), 633–638.
1409 https://doi.org/10.1094/PDIS.2002.86.6.633
1410 Meidanis, J., Braga, M. D. V., & Verjovski-Almeida, S. (2002). Whole-genome analysis of
1411 transporters in the plant pathogen *Xylella fastidiosa*. *Microbiology and Molecular*
1412 *Biology Reviews*, *66*(2), 272–299. https://doi.org/10.1128/MMBR.66.2.272-299.2002
1413 Mirhakkak, M. H., Chen, X., Ni, Y., Heinekamp, T., Sae-Ong, T., Xu, L.-L., Kurzai, O., Barber,
1414 A. E., Brakhage, A. A., Boutin, S., Schäuble, S., & Panagiotou, G. (2023). Genome-
1415 scale metabolic modeling of *Aspergillus fumigatus* strains reveals growth
1416 dependencies on the lung microbiome. *Nature Communications*, *14*(1), 4369.
1417 https://doi.org/10.1038/s41467-023-39982-5
1418 Mistry, J., Chuguransky, S., Williams, L., Qureshi, M., Salazar, G. A., Sonnhammer, E. L. L.,
1419 Tosatto, S. C. E., Paladin, L., Raj, S., Richardson, L. J., Finn, R. D., & Bateman, A.
1420 (2021). Pfam: The protein families database in 2021. *Nucleic Acids Research*, *49*(D1),
1421 D412–D419. https://doi.org/10.1093/nar/gkaa913

Mistry, J., Finn, R. D., Eddy, S. R., Bateman, A., & Punta, M. (2013). Challenges in homology search: HMMER3 and convergent evolution of coiled-coil regions. *Nucleic Acids Research*, *41*(12), e121. https://doi.org/10.1093/nar/gkt263

Monk, J., Nogales, J., & Palsson, B. O. (2014). Optimizing genome-scale network reconstructions. *Nature Biotechnology*, *32*(5), 447–452. https://doi.org/10.1038/nbt.2870

Nakahigashi, K., Toya, Y., Ishii, N., Soga, T., Hasegawa, M., Watanabe, H., Takai, Y., Honma, M., Mori, H., & Tomita, M. (2009). Systematic phenome analysis of *Escherichia coli* multiple-knockout mutants reveals hidden reactions in central carbon metabolism. *Molecular Systems Biology*, *5*(1), MSB200965. https://doi.org/10.1038/msb.2009.65

Nascimento, R., Gouran, H., Chakraborty, S., Gillespie, H. W., Almeida-Souza, H. O., Tu, A., Rao, B. J., Feldstein, P. A., Bruening, G., Goulart, L. R., & Dandekar, A. M. (2016). The type II secreted lipase/esterase LesA is a key virulence factor required for *Xylella fastidiosa* pathogenesis in grapevines. *Scientific Reports*, *6*(1), 18598. https://doi.org/10.1038/srep18598

Neumann, M. (2003). Sequence tag analysis of gene expression during pathogenic growth and microsclerotia development in the vascular wilt pathogen *Verticillium dahliae*. *Fungal Genetics and Biology*, *38*(1), 54–62. https://doi.org/10.1016/S1087-1845(02)00507-8

Nogales, J. (2017). A practical protocol for genome-scale metabolic reconstructions. In T. J. McGenity, K. N. Timmis, & B. Nogales (Eds), *Hydrocarbon and lipid microbiology protocols: genetic, genomic and system analyses of pure cultures* (pp. 197–221). Springer. https://doi.org/10.1007/8623_2014_12

Norsigian, C. J., Fang, X., Seif, Y., Monk, J. M., & Palsson, B. O. (2020). A workflow for generating multi-strain genome-scale metabolic models of prokaryotes. *Nature Protocols*, *15*(1), 1–14. https://doi.org/10.1038/s41596-019-0254-3

O'Brien, E. J., Monk, J. M., & Palsson, B. O. (2015). Using genome-scale models to predict biological capabilities. *Cell*, *161*(5), 971–987. https://doi.org/10.1016/j.cell.2015.05.019

Oliveira, A., Cunha, E., Silva, M., Faria, C., & Dias, O. (2023). Exploring *Xylella fastidiosa*'s metabolic traits using a GSM model of the phytopathogenic bacterium. In F. Fdez-Riverola, M. Rocha, M. S. Mohamad, S. Caraiman, & A. B. Gil-González (Eds), *Practical Applications of Computational Biology and Bioinformatics, 16th International Conference (PACBB 2022)* (Vol. 553, pp. 79–88). Springer International Publishing. https://doi.org/10.1007/978-3-031-17024-9_8

Orth, J. D., Conrad, T. M., Na, J., Lerman, J. A., Nam, H., Feist, A. M., & Palsson, B. Ø. (2011).

A comprehensive genome-scale reconstruction of *Escherichia coli* metabolism—2011. *Molecular Systems Biology*, *7*(1), 535. https://doi.org/10.1038/msb.2011.65

Orth, J. D., Thiele, I., & Palsson, B. Ø. (2010). What is flux balance analysis? *Nature Biotechnology*, *28*(3), 245–248. https://doi.org/10.1038/nbt.1614

Overbeek, R., Begley, T., Butler, R. M., Choudhuri, J. V., Chuang, H.-Y., Cohoon, M., de Crécy-Lagard, V., Diaz, N., Disz, T., Edwards, R., Fonstein, M., Frank, E. D., Gerdes, S., Glass, E. M., Goesmann, A., Hanson, A., Iwata-Reuyl, D., Jensen, R., Jamshidi, N., … Vonstein, V. (2005). The subsystems approach to genome annotation and its use in the project to annotate 1000 genomes. *Nucleic Acids Research*, *33*(17), 5691–5702. https://doi.org/10.1093/nar/gki866

Palsson, B. Ø. (2015). *Systems Biology: Constraint-based reconstruction and analysis*. Cambridge University Press. https://doi.org/10.1017/CBO9781139854610

Peyraud, R., Cottret, L., Marmiesse, L., Gouzy, J., & Genin, S. (2016). A Resource Allocation Trade-Off between Virulence and Proliferation Drives Metabolic Versatility in the Plant Pathogen Ralstonia solanacearum. *PLOS Pathogens*, *12*(10), e1005939. https://doi.org/10.1371/journal.ppat.1005939

PM 7/24 (5) Xylella fastidiosa. (2023). *EPPO Bulletin*, *53*(2), 205–276. https://doi.org/10.1111/epp.12923

Ponce-de-Leon, M., Calle-Espinosa, J., Peretó, J., & Montero, F. (2015). Consistency analysis of genome-scale models of bacterial metabolism: A metamodel approach. *PLOS ONE*, *10*(12), e0143626. https://doi.org/10.1371/journal.pone.0143626

Purcino, R. P., Medina, C. L., Martins de Souza, D., Winck, F. V., Machado, E. C., Novello, J. C., Machado, M. A., & Mazzafera, P. (2007). *Xylella fastidiosa* disturbs nitrogen metabolism and causes a stress response in sweet orange *Citrus sinensis* cv. Pera. *Journal of Experimental Botany*, *58*(11), 2733–2744. https://doi.org/10.1093/jxb/erm138

Qian, J., & Ye, C. (2024). Development and applications of genome-scale metabolic network models. In *Advances in Applied Microbiology* (Vol. 126, pp. 1–26). Academic Press. https://doi.org/10.1016/bs.aambs.2024.02.002

Remm, M., Storm, C. E. V., & Sonnhammer, E. L. L. (2001). Automatic clustering of orthologs and in-paralogs from pairwise species comparisons. *Journal of Molecular Biology*, *314*(5), 1041–1052. https://doi.org/10.1006/jmbi.2000.5197

Román-Écija, M., Navas-Cortés, J. A., Velasco-Amo, M. P., Arias-Giraldo, L. F., Gómez, L. M., Fuente, L. D. L., & Landa, B. B. (2023). Two *Xylella fastidiosa* subsp. *multiplex* strains isolated from almond in spain differ in plasmid content and virulence traits. *Phytopathology®*, *113*(6), 960–974. https://doi.org/10.1094/PHYTO-06-22-0234-R

Sanchez, F. B., Barreiro, H. J., Soto, E. I., & Rodriguez, C. E. (2019). *The Impact Indicator for Priority Pests (I2P2): A tool for ranking pests according to Regulation (EU) 2016/2031*. Publications Office of the European Union. https://doi.org/10.2760/585182

Santos, A. P., Muratore, L. N., Solé-Gil, A., Farías, M. E., Ferrando, A., Blázquez, M. A., & Belfiore, C. (2021). Extremophilic bacteria restrict the growth of *Macrophomina phaseolina* by combined secretion of polyamines and lytic enzymes. *Biotechnology Reports*, *32*, e00674. https://doi.org/10.1016/j.btre.2021.e00674

Sayers, E. W., Beck, J., Bolton, E. E., Brister, J. R., Chan, J., Connor, R., Feldgarden, M., Fine, A. M., Funk, K., Hoffman, J., Kannan, S., Kelly, C., Klimke, W., Kim, S., Lathrop, S., Marchler-Bauer, A., Murphy, T. D., O'Sullivan, C., Schmieder, E., … Pruitt, K. D. (2024). Database resources of the National Center for Biotechnology Information in 2025. *Nucleic Acids Research*, *53*(D1), D20–D29. https://doi.org/10.1093/nar/gkae979

Scala, V., Salustri, M., Merfa, M. V., Beccaccioli, M., Lascala, L., De La Fuente, L., & Reverberi, M. (2025). XadA-like adhesin XADA2 regulates biofilm formation in *X. fastidiosa* subsp. *fastidiosa* putatively by engaging oleic-acid derived oxylipins. *Molecular Biology Reports*, *52*(1), 263. https://doi.org/10.1007/s11033-025-10259-y

Scally, M., Schuenzel, E. L., Stouthamer, R., & Nunney, L. (2005). Multilocus sequence type system for the plant pathogen *Xylella fastidiosa* and relative contributions of recombination and point mutation to clonal diversity. *Applied and Environmental Microbiology*, *71*(12), 8491–8499. https://doi.org/10.1128/AEM.71.12.8491-8499.2005

Schada von Borzyskowski, L., Bernhardsgrütter, I., & Erb, T. J. (2020). Biochemical unity revisited: Microbial central carbon metabolism holds new discoveries, multi-tasking pathways, and redundancies with a reason. *Biological Chemistry*, *401*(12), 1429–1441. https://doi.org/10.1515/hsz-2020-0214

Schatschneider, S., Persicke, M., Watt, S. A., Hublik, G., Pühler, A., Niehaus, K., & Vorhölter, F.-J. (2013). Establishment, in silico analysis, and experimental verification of a large-scale metabolic network of the xanthan producing *Xanthomonas campestris* pv. campestris strain B100. *Journal of Biotechnology*, *167*(2), 123–134. https://doi.org/10.1016/j.jbiotec.2013.01.023

Segura, D., Mahadevan, R., Juárez, K., & Lovley, D. R. (2008). Computational and Experimental analysis of redundancy in the central metabolism of *Geobacter sulfurreducens*. *PLOS Computational Biology*, *4*(2), e36. https://doi.org/10.1371/journal.pcbi.0040036

Shannon, P., Markiel, A., Ozier, O., Baliga, N. S., Wang, J. T., Ramage, D., Amin, N., Schwikowski, B., & Ideker, T. (2003). Cytoscape: A software environment for integrated models of biomolecular interaction networks. *Genome Research*, *13*(11),

2498–2504. https://doi.org/10.1101/gr.1239303

Simko, I., & Piepho, H.-P. (2012). The area under the disease progress stairs: Calculation, advantage, and application. *Phytopathology®*, *102*(4), 381–389. https://doi.org/10.1094/PHYTO-07-11-0216

Simpson, A. J., Reinach, F. C., Arruda, P., Abreu, F. A., Acencio, M., Alvarenga, R., Alves, L. M., Araya, J. E., Baia, G. S., Baptista, C. S., Barros, M. H., Bonaccorsi, E. D., Bordin, S., Bové, J. M., Briones, M. R., Bueno, M. R., Camargo, A. A., Camargo, L. E., Carraro, D. M., … Setubal, J. C. (2000). The genome sequence of the plant pathogen *Xylella fastidiosa*. *Nature*, *406*(6792), 151–157. https://doi.org/10.1038/35018003

Solé-Gil, A., Hernández-García, J., López-Gresa, M. P., Blázquez, M. A., & Agustí, J. (2019). Conservation of thermospermine synthase activity in vascular and non-vascular plants. *Frontiers in Plant Science*, *10*. https://doi.org/10.3389/fpls.2019.00663

Solmi, L., Rossi, F. R., Romero, F. M., Bach-Pages, M., Preston, G. M., & Gárriz, A. (2025). The influence of the polyamine synthesis pathways on *Pseudomonas syringae* virulence and plant interaction. *Microbiology*, *171*(6), 001569. https://doi.org/10.1099/mic.0.001569

Sugiyama, Y., Nara, M., Sakanaka, M., Gotoh, A., Kitakata, A., Okuda, S., & Kurihara, S. (2017). Comprehensive analysis of polyamine transport and biosynthesis in the dominant human gut bacteria: Potential presence of novel polyamine metabolism and transport genes. *The International Journal of Biochemistry & Cell Biology*, *93*, 52–61. https://doi.org/10.1016/j.biocel.2017.10.015

Surano, A., del Grosso, C., Musio, B., Todisco, S., Giampetruzzi, A., Altamura, G., Saponari, M., Gallo, V., Mastrorilli, P., Boscia, D., & Saldarelli, P. (2024). Exploring the xylem-sap to unravel biological features of *Xylella fastidiosa* subspecies *pauca* ST53 in immune, resistant and susceptible crop species through metabolomics and in vitro studies. *Frontiers in Plant Science*, *14*. https://doi.org/10.3389/fpls.2023.1343876

Tabuchi, T., Serizawa, N., & Uchiyama, H. (1974). A novel pathway for the partial oxidation of propionyl-coa to pyruvate *via* seven-carbon tricarboxylic acids in yeasts. *Agricultural and Biological Chemistry*, *38*(12), 2571–2572. https://doi.org/10.1080/00021369.1974.10858334

Thiele, I., & Palsson, B. Ø. (2010). A protocol for generating a high-quality genome-scale metabolic reconstruction. *Nature Protocols*, *5*(1), 93–121. https://doi.org/10.1038/nprot.2009.203

UniProt Consortium. (2025). UniProt: The Universal Protein Knowledgebase in 2025. *Nucleic Acids Research*, *53*(D1), D609–D617. https://doi.org/10.1093/nar/gkae1010

Vanhove, M., Retchless, A. C., Sicard, A., Rieux, A., Coletta-Filho, H. D., De La Fuente, L.,

Stenger, D. C., & Almeida, R. P. P. (2019). Genomic diversity and recombination among *Xylella fastidiosa* subspecies. *Applied and Environmental Microbiology*, *85*(13), e02972-18. https://doi.org/10.1128/AEM.02972-18

Wang, P., Lee, Y., Igo, M. M., & Roper, M. C. (2017). Tolerance to oxidative stress is required for maximal xylem colonization by the xylem-limited bacterial phytopathogen, *Xylella fastidiosa*. *Molecular Plant Pathology*, *18*(7), 990–1000. https://doi.org/10.1111/mpp.12456

Wells, J. M., Raju, B. C., Hung, H.-Y., Weisburg, W. G., Mandelco-Paul, L., & Brenner, D. J. (1987). *Xylella fastidiosa* gen. nov., sp. nov: Gram-negative, xylem-limited, fastidious plant bacteria related to *Xanthomonas* spp. *International Journal of Systematic and Evolutionary Microbiology*, *37*(2), 136–143. https://doi.org/10.1099/00207713-37-2-136

Wells, J. M., Raju, B. C., Nyland, G., & Lowe, S. K. (1981). Medium for isolation and growth of bacteria associated with plum leaf scald and phony peach diseases. *Applied and Environmental Microbiology*, *42*(2), 357–363. https://doi.org/10.1128/aem.42.2.357-363.1981

Ye, C., Wei, X., Shi, T., Sun, X., Xu, N., Gao, C., & Zou, W. (2022). Genome-scale metabolic network models: From first-generation to next-generation. *Applied Microbiology and Biotechnology*, *106*(13), 4907–4920. https://doi.org/10.1007/s00253-022-12066-y

Youssefi, F., Brown, P., & Weinbaum, S. (2000). Relationship between tree nitrogen status, xylem and phloem sap amino acid concentrations, and apparent soil nitrogen uptake by almond trees *(Prunus dulcis)*. *The Journal of Horticultural Science and Biotechnology*, *75*(1), 62–68. https://doi.org/10.1080/14620316.2000.11511201

Yus, E., Maier, T., Michalodimitrakis, K., van Noort, V., Yamada, T., Chen, W.-H., Wodke, J. A. H., Güell, M., Martínez, S., Bourgeois, R., Kühner, S., Raineri, E., Letunic, I., Kalinina, O. V., Rode, M., Herrmann, R., Gutiérrez-Gallego, R., Russell, R. B., Gavin, A.-C., … Serrano, L. (2009). Impact of genome reduction on bacterial metabolism and its regulation. *Science*, *326*(5957), 1263–1268. https://doi.org/10.1126/science.1177263

yWorks GmbH (2020). *yEd Graph Editor* (Version 3.18.2) [Computer software]. https://www.yworks.com/products/yed

Zarzycki, J., & Fuchs, G. (2011). Coassimilation of organic substrates via the autotrophic 3-hydroxypropionate bi-cycle in *Chloroflexus aurantiacus*. *Applied and Environmental Microbiology*, *77*(17), 6181–6188. https://doi.org/10.1128/AEM.00705-11

Zhu, G., Golding, G. B., & Dean, A. M. (2005). The selective cause of an ancient adaptation. *Science*, *307*(5713), 1279–1282. https://doi.org/10.1126/science.1106974

1602

1603 ## Figure Legends

1604

1605 **Figure 1. Genome-scale metabolic model reconstruction of *Xylella fastidiosa* through a**
1606 **pangenome based on the subspecies *pauca*, *multiplex*, *fastidiosa*, *morus* and *sandyi*.**
1607 A) Pangenome analysis illustrating the distribution of core genes, genes shared between
1608 subspecies and unique genes. Each bar in the vertical bar chart represents the number of
1609 ortholog groups shared by the strains indicated below the chart. B) Summary of the features
1610 (reactions, metabolites and genes) from the *X. fastidiosa* metabolic core (Xfcore)
1611 reconstructed in this work. C) Predicted flux distribution through the core metabolism, using
1612 FBA, in a minimal medium with glutamine as the sole carbon and nitrogen source, achieving
1613 a specific growth rate of 0.41 h^{-1}. Metabolic fluxes ($mmol \cdot gDW^{-1} \cdot h^{-1}$) are portrayed
1614 numerically.

1615

1616 **Figure 2. Evaluation of six synthetic defined growth media based on Xfcore model**
1617 **predictions**. Total bacterial growth measured by the standardized area under the growth
1618 progress curve (sAUGPC) (A) and biofilm formation (B) of seven *X. fastidiosa* strains grow at
1619 28 °C for 6 days. PD3 medium is included as a positive control. Statistical differences between
1620 each synthetic defined medium and the PD3 control were assessed using Wilcoxon rank-sum
1621 tests. Significance levels of comparisons are displayed above each line connecting group pairs
1622 (ns: $P>0.05$, *: $P\leq0.05$, **: $P\leq0.01$, ***: $P\leq0.001$, ****: $P\leq0.0001$).

1623

1624 **Figure 3. Predicted acetate assimilation by the Xfcore model.** Flux distribution through the
1625 *X. fastidiosa* core metabolism, using FBA, in medium with acetate as the sole carbon and
1626 glutamic acid and ammonium as nitrogen source, achieving a specific growth rate of 1.14 h^{-1}.
1627 Metabolic fluxes ($mmol \cdot gDW^{-1} \cdot h^{-1}$) are portrayed numerically. The alternative metabolic
1628 strategy for converting acetate into biomass combines two previously described modules: half
1629 of the 3-hydroxypropionate (3HP) bicycle (Herter et al., 2002) and the methylcitrate pathway
1630 (Brämer & Steinbüchel, 2001; Dolan et al., 2018) for propionyl-CoA assimilation. The enzymes
1631 and genes involved in the metabolic steps (1-11) of this pathway are in Supplementary Table
1632 S4. Abbreviations for metabolites participating in the 3HP pathway and the methylcitrate
1633 pathway: MCOA (malonyl CoA), MSA (malonate semialdehyde or 3-oxopropanoate), 3HP (3-

1634 hydroxypropionate), 3HPCOA (3-hrydroxypropionyl CoA), PP2COA (acryloyl CoA), PPCOA
1635 (propionyl CoA), 2MCIT (2-methylcitrate), 2MCACN (2-methylaconitate), MICT (2-
1636 methylisocitrate).

1637

1638 **Figure 4. Polyamine production by *Xylella fastidiosa.*** A) Trade-off between biomass and
1639 polyamine production using the Xcore model. This figure illustrates the inverse relationship
1640 between growth (biomass accumulation) and the production of polyamines (putrescine,
1641 spermidine, and spermine) when one of the polyamines is completely absent. Simulations
1642 were performed using a minimal medium where glutamine served as the sole carbon source
1643 (with an uptake flux of 15.665 $mmol \cdot gDW^{-1} \cdot h^{-1}$). For each data point, the biomass reaction
1644 was maximized while the production fluxes for the polyamines (putrescine, spermidine, and
1645 spermine) were incrementally forced to the values represented by axis in flux units,
1646 $mmol \cdot gDW^{-1} \cdot h^{-1}$. A minimal threshold of 0.1608 $mmol \cdot gDW^{-1} \cdot h^{-1}$ was established for the
1647 consideration of growth. B) In vitro production of putrescine, spermidine and spermine across
1648 different sample types (cell pellet from biofilm, CP-B; cell pellet from planktonic growth, CP-P;
1649 and culture supernatant, SP). Samples were obtained from three *Xylella fastidiosa* strains (De
1650 Donno, ESVL and Temecula1) grown at 28 °C in PD3 medium for 5 and 12 days, with four
1651 replicates for each sample and time point. Concentrations (in $ng \cdot mL^{-1}$) are visualized with a
1652 pseudo-logarithmic scale. Statistical differences between time points within each sample type
1653 and strain were assessed using Wilcoxon rank-sum tests. Only significant results are indicated
1654 ($*$: $P \leq 0.05$).

1655

1656 **Figure 5. Trade-off between biomass and virulence factor production in *X. fastidiosa.***
1657 This figure illustrates the inverse relationship between growth (biomass accumulation) and the
1658 production of: LesA protein, fastidian gum EPS, and putrescine (A), spermidine (B) or
1659 spermine (C) using the Xfcore metabolic mode, when one of the three compounds is
1660 completely absent. Simulations were performed using a minimal medium where glutamine
1661 served as the sole carbon source (with an uptake flux of 15.664 $mmol \cdot gDW^{-1} \cdot h^{-1}$). For each
1662 data point, the biomass reaction was maximized while the production fluxes for the virulence
1663 factors (LesA, EPS, polyamine) were incrementally forced to the values represented by the
1664 axis in flux units, $mmol \cdot gDW^{-1} \cdot h^{-1}$. A minimal threshold of 0.1608 $mmol \cdot gDW^{-1} \cdot h^{-1}$ was
1665 established for the consideration of growth.

1666

1667 ## Table legends

1668 **Table 1. Summary of *X. fastidiosa* strains used for the pangenome reconstruction and**
1669 **genome-scale metabolic modeling.**

1670

1671 **Table 2. Comparison between in silico growth predictions and in vitro phenotypic**
1672 **profiles of *X. fastidiosa*.** Experimental growth across various substrates, including
1673 carbohydrates, organic acids, lipids, and amino acids, was obtained from Biolog PM plates. In
1674 silico growth was predicted through FBA using the Xfcore model as described in Material and
1675 Methods.

Fig. 1

A

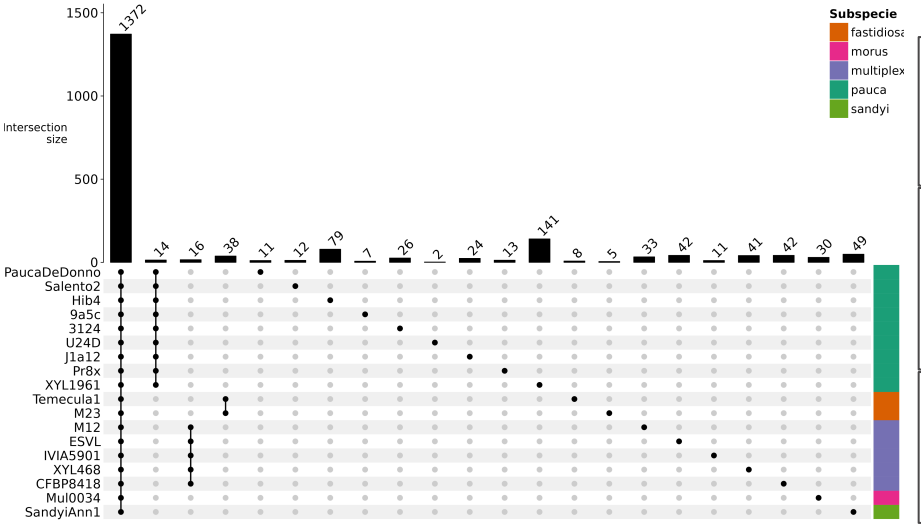

B

	iXfcore features	Count
Metabolites	Cytosol metabolites	1012
	Extracellular metabolites	63
	Unique metabolites	1013
	Total	1075
Reactions	Boundary reactions	69
	Transport reactions	76
	Biomass reactions	1
	Biochemical reactions	964 (888)
	Total	1034
Genes	Core genes	407
	Accessory genes	43
	Others	1
	Total	451

C

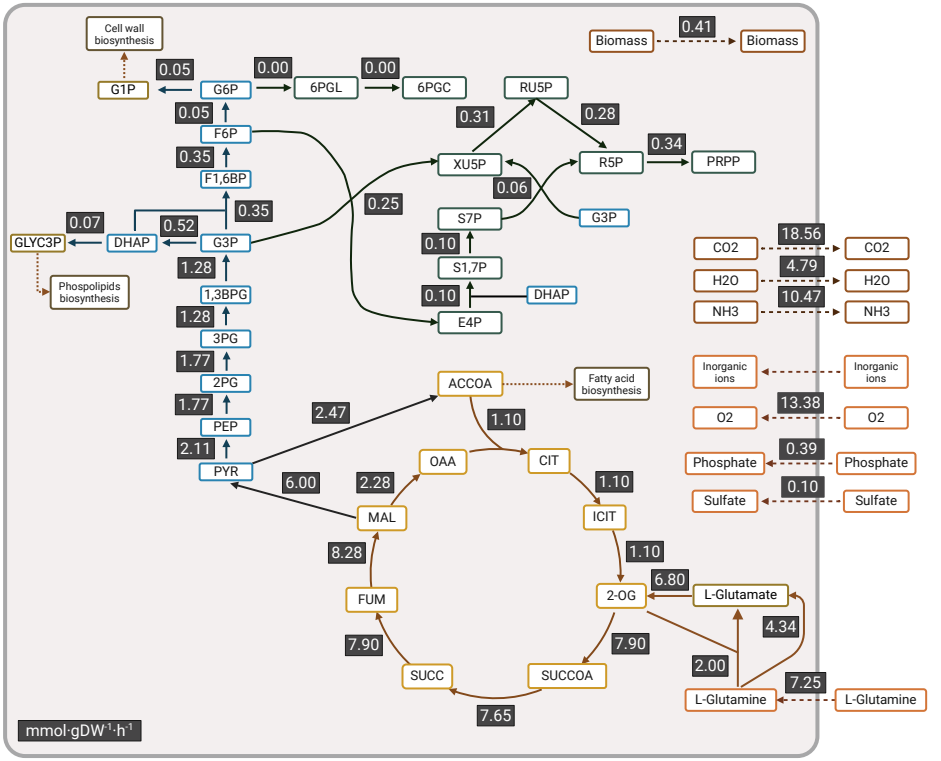

Fig. 2

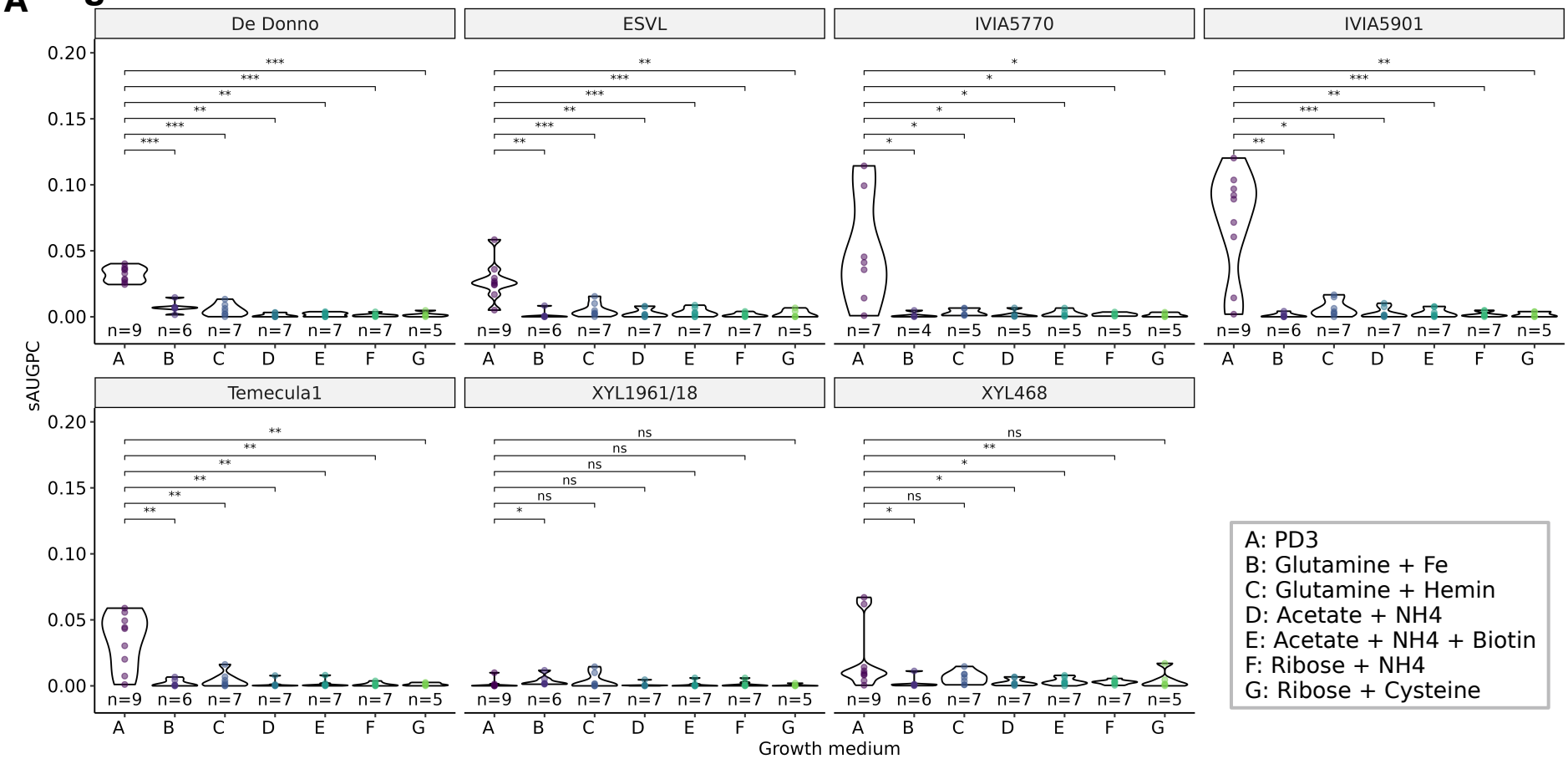
A
De Donno
ESVL
IVIA5770
IVIA5901
Temecula1
XYL1961/18
XYL468
sAUGPC
0.20
0.15
0.10
0.05
0.00
n=9 n=6 n=7 n=7 n=7 n=7 n=5
n=7 n=4 n=5 n=5 n=5 n=5 n=5
A B C D E F G
Growth medium
A: PD3
B: Glutamine + Fe
C: Glutamine + Hemin
D: Acetate + NH4
E: Acetate + NH4 + Biotin
F: Ribose + NH4
G: Ribose + Cysteine

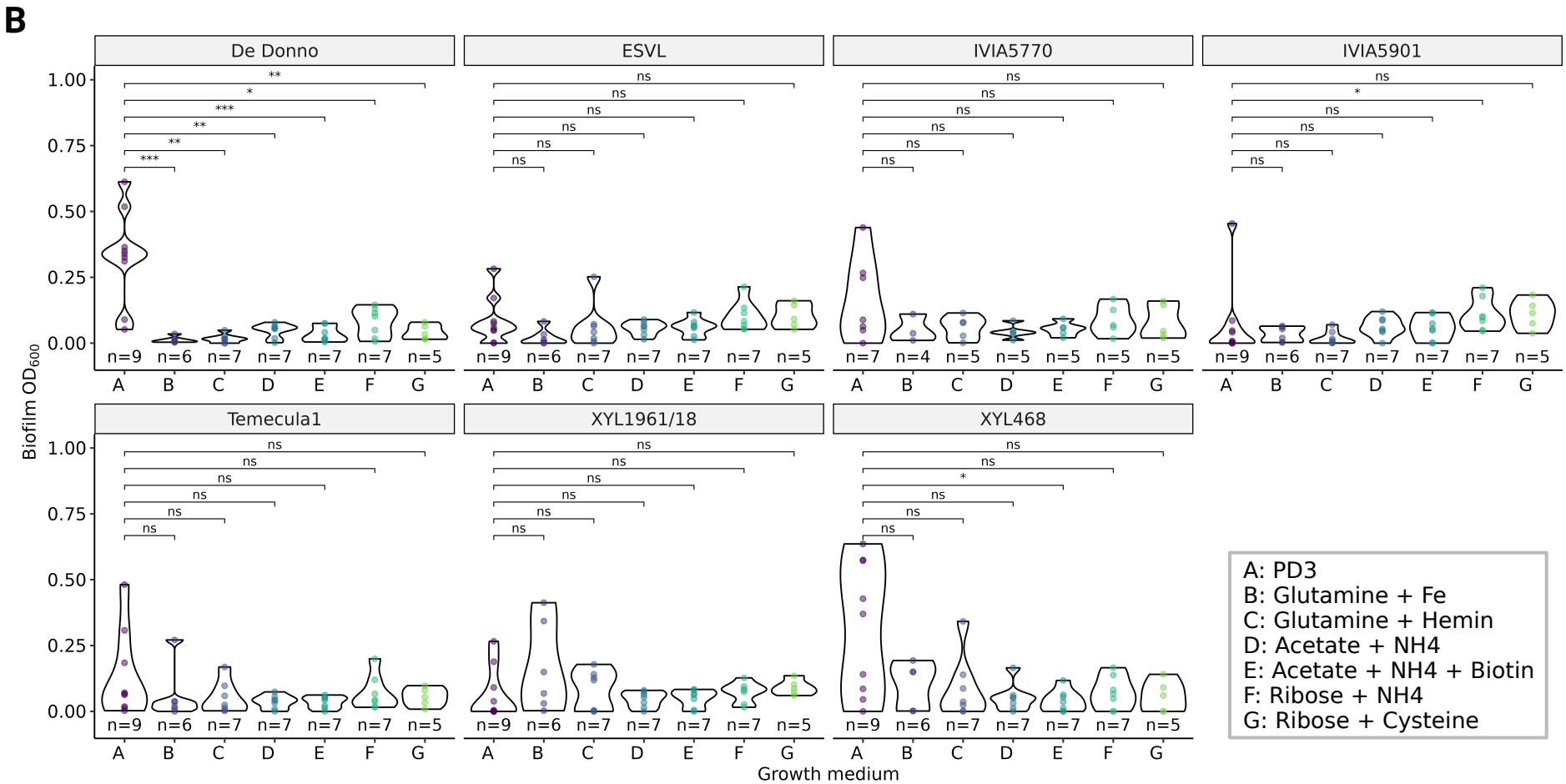
B
De Donno
ESVL
IVIA5770
IVIA5901
Temecula1
XYL1961/18
XYL468
Biofilm OD600
1.00
0.75
0.50
0.25
0.00
n=9 n=6 n=7 n=7 n=7 n=7 n=5
n=7 n=4 n=5 n=5 n=5 n=5 n=5
A B C D E F G
Growth medium
A: PD3
B: Glutamine + Fe
C: Glutamine + Hemin
D: Acetate + NH4
E: Acetate + NH4 + Biotin
F: Ribose + NH4
G: Ribose + Cysteine

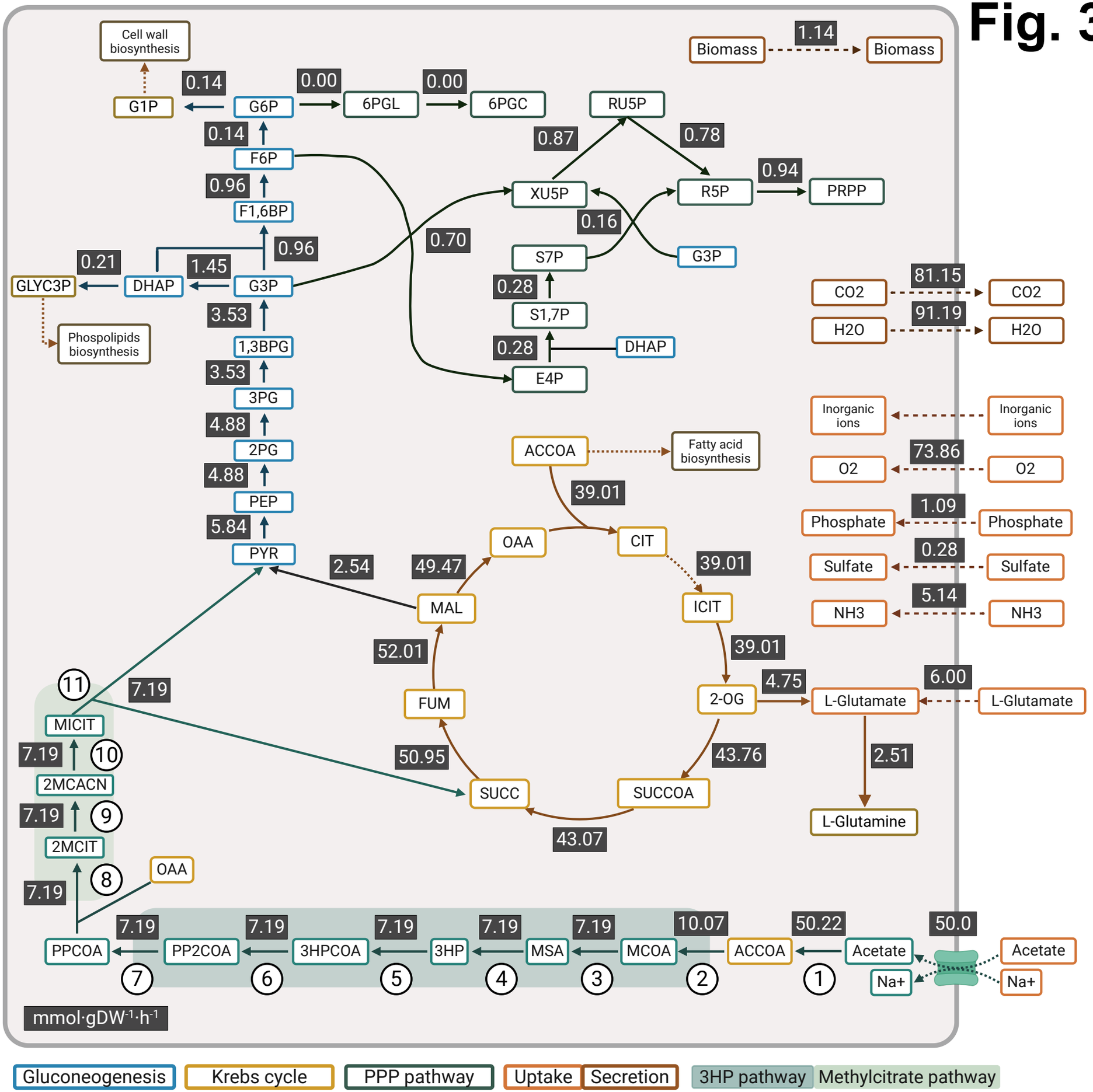
Fig. 3
Cell wall biosynthesis
G1P
0.14
G6P
0.00
6PGL
0.00
6PGC
Biomass
1.14
Biomass
RU5P
0.87
0.78
0.14
F6P
0.96
F1,6BP
XU5P
R5P
0.94
PRPP
0.16
0.70
0.96
S7P
G3P
0.21
1.45
GLYC3P
DHAP
G3P
0.28
S1,7P
3.53
Phospolipids biosynthesis
1,3BPG
0.28
DHAP
E4P
3.53
3PG
4.88
2PG
4.88
PEP
5.84
PYR
CO2
81.15
CO2
H2O
91.19
H2O
Inorganic ions
Inorganic ions
O2
73.86
O2
Phosphate
1.09
Phosphate
Sulfate
0.28
Sulfate
NH3
5.14
NH3
ACCOA
Fatty acid biosynthesis
39.01
OAA
CIT
39.01
2.54
49.47
MAL
ICIT
52.01
39.01
11
7.19
FUM
2-OG
4.75
6.00
L-Glutamate
L-Glutamate
MICIT
7.19
10
50.95
43.76
2.51
2MCACN
SUCC
SUCCOA
7.19
9
L-Glutamine
2MCIT
43.07
OAA
8
7.19
7.19
7.19
7.19
7.19
10.07
50.22
50.0
PPCOA
PP2COA
3HPCOA
3HP
MSA
MCOA
ACCOA
Acetate
Acetate
7
6
5
4
3
2
1
Na+
Na+
mmol·gDW-1·h-1
Gluconeogenesis
Krebs cycle
PPP pathway
Uptake
Secretion
3HP pathway
Methylcitrate pathway

Fig. 4

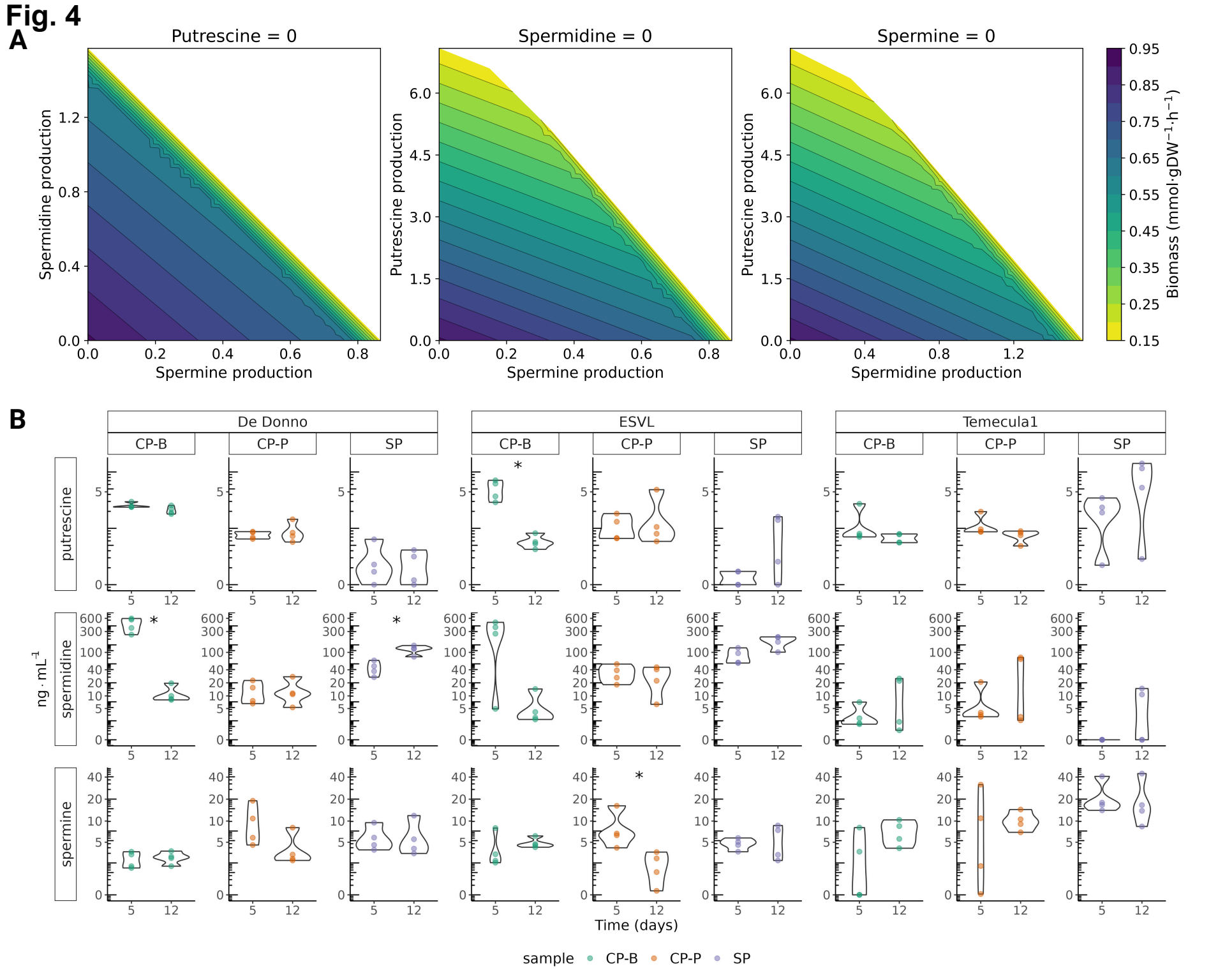
A
Putrescine = 0
Spermidine = 0
Spermine = 0
Spermidine production
Putrescine production
Spermine production
Spermidine production
Biomass (mmol·gDW⁻¹·h⁻¹)
B
De Donno
ESVL
Temecula1
CP-B
CP-P
SP
putrescine
spermidine
spermine
ng · mL⁻¹
Time (days)
sample
CP-B
CP-P
SP

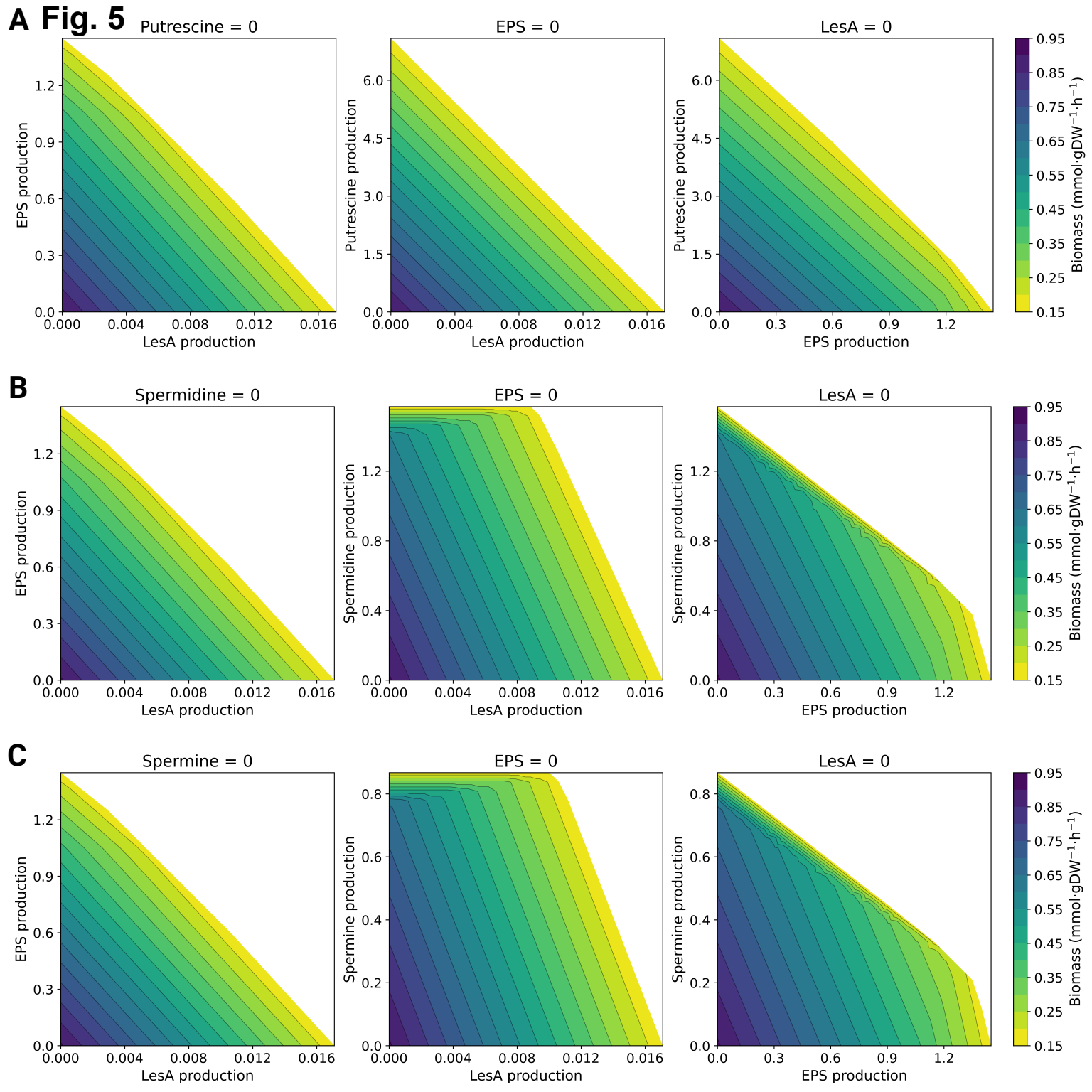
A Fig. 5
Putrescine = 0
EPS = 0
LesA = 0
EPS production
Putrescine production
LesA production
EPS production
Biomass (mmol·gDW^{-1}·h^{-1})
B
Spermidine = 0
EPS = 0
LesA = 0
EPS production
Spermidine production
LesA production
EPS production
Biomass (mmol·gDW^{-1}·h^{-1})
C
Spermine = 0
EPS = 0
LesA = 0
EPS production
Spermine production
LesA production
EPS production
Biomass (mmol·gDW^{-1}·h^{-1})

Table 1.

Identifier	Subspecies	Host	Location	Disease[a]	ID RefSeq
Temecula1	*fastidiosa*	*Vitis vinifera*	California, USA	PD	NC_004556.1
M23	*fastidiosa*	*Prunus dulcis*	California, USA	PD, ALS	NC_010577.1
MUL0034	*morus*	*Morus alba*	California, USA	MLS	NZ_CP006740.1
M12	*multiplex*	*Prunus dulcis*	California, USA	ALS	NC_010513.1
9a5c	*pauca*	*Citrus sinensis*	São Paulo, Brazil	CVC	NC_002488.3
U24d	*pauca*	*Citrus sinensis*	São Paulo, Brazil	CVC	NZ_CP009790.1
J1a12	*pauca*	*Citrus sinensis*	São Paulo, Brazil	Non-pathogenic	NZ_CP009823.1
Pr8x	*pauca*	*Prunus domestica*	São Paulo, Brazil	LS	NZ_CP009826.1
3124	*pauca*	*Coffee arabica*	São Paulo, Brazil	CLS	NZ_CP009829.1
Hib4	*pauca*	*Hibiscus fragilis*	Distrito Federal, Brazil	LS	NZ_CP009885.1
Salento-2	*pauca*	*Olea europaea*	Puglia, Italy	OQDS	NZ_CP016610.1
De Donno	*pauca*	*Olea europaea*	Puglia, Italy	OQDS	NZ_CP020870.1
Ann-1	*sandyi*	*Nerium oleander*	California, USA	OLS	NZ_CP006696.1
ESVL	*multiplex*	*Prunus dulcis*	Alicante, Spain	ALS	NZ_CP099516.1
IVIA5901	*multiplex*	*Prunus dulcis*	Alicante, Spain	ALS	NZ_CP047134.1
XYL1961/18	*pauca*	*Olea europaea var. europaea*	Ibiza, Spain	OQDS	CP171775.1
XYL468	*multiplex*	*Olea europaea var. sylvestris*	Mallorca, Spain	OQDS	NZ_CP136966.1
CFBP8418	*multiplex*	*Spartium junceum*	Corse, France	LS	NZ_CP136979.1

[a] PD: Pierce's Disease; ALS: Almond Leaf Scorch; MLS: Mulberry Leaf Scorch; CVC: Citrus Variegated Chlorosis; CLS: Coffee Leaf Scorch; OQDS: Olive Quick Decline Syndrome; OLS: Oleander Leaf Scorch; LS: Leaf Scorch.

Table 2.

Substrate	Growth assessment	
	In silico[a]	**Experimental**
Carbohydrates and derivatives		
D-Ribose	+	+
D-Xylose	+	+
L-Arabinose	-	+
L-Lyxose	-	+
2-Deoxy-D-Ribose	-	+
D-Arabinose	n.a.	+
D-Fructose-6-Phosphate	+	+
D-Psicose	-	+
D-Tagatose	-	+
L-Sorbose	n.a.	+
L-Rhamnose	n.a.	+
Inulin	n.a.	+
Pectin	n.a.	+
D-Glucosamine	+	+
3-0-β-D-Galactopyranosyl-D-Arabinose	n.a.	+
Glucuronamide	n.a.	+
L-Galactonic Acid-γ-Lactone	n.a.	+
5-Keto-D-Gluconic Acid	n.a.	+
Organic acids		
∝-Keto-Glutaric Acid	+	+
∝-Keto-Butyric Acid	-	+
∝-Keto-Valeric Acid	n.a.	+
Pyruvic acid	+	+
Acetoacetic Acid	-	+

Acetic Acid	+	+
Oxalic Acid	n.a.	+
Oxalomalic Acid	n.a.	+
Dihydroxy Acetone	-	+
Sorbic Acid	n.a.	+
Lipids and fatty acids		
Capric acid	n.a.	+
Tween 20	n.a.	+
Tween 40	n.a.	+
D,L-Carnitine	n.a.	+
Amino acids and amines		
Tyramine	n.a.	+
Sec-Butylamine	n.a.	+

[a] (+) and (-) indicate, respectively, growth/no growth in the corresponding simulation or experimental result. (n.a.) indicates metabolites not represented in the metabolic reconstruction or not available to model.